


Engineering fibroblast with reprogramming and spheronization for bone defect repair

Yanjiao Li^{a,1}, Bin Jiang^{b,1}, Zhen Wu^c, Zhaoxia Ma^a, Lihua Qiu^a, Wen Cui^{d,e}, Yunhui Zhao^d, Jinghe Yan^{a,f}, Daiping Ma^c, Xingfei Wu^{d,e}, Shu Liang^d, Sitao Wang^d, Yanqun Zhao^d, Mengting Wang^c, Min Hu^{a,*} 

^a Yunnan Key Laboratory for Basic Research on Bone and Joint Diseases, Kunming University, Kunming, Yunnan, 650214, China

^b R&D Division, Eureka Biotech Inc., Philadelphia, PA, United States

^c Shenzhen Zhendejici Pharmaceutical Research and Development Co., Ltd., Shenzhen, Guangdong, 518048, China

^d Yunnan Jici Institute for Regenerative Medicine Co., Ltd., Kunming, Yunnan, 650101, China

^e Guangzhou Dayi Pharmaceutical Research Co., Ltd., Guangzhou, Guangdong, 511400, China

^f Centre for Host-Microbiome Interactions, Faculty of Dental, Oral & Craniofacial Sciences, King's College London, London, SE1 9RT, UK

ARTICLE INFO

Keywords:

Engineering fibroblast
Elderly autologous induced osteoblast
Spheroid
Endogenous revascularization and osteogenesis
High productivity and survival

ABSTRACT

Bone diseases profoundly affect patients, particularly the elderly, leading to severe health complications and disabilities. Osteoblasts play a crucial role in bone formation and are ideal candidates for treating bone diseases and engineering living materials. However, the stem and progenitor cells that give rise to osteoblasts, as well as osteoblasts themselves, exhibit dysfunction with aging. Although chemical reprogramming of fibroblasts into osteoblasts has been achieved, effective cell-based therapies or living materials have not been established in clinical practice. Here, we present a method to engineer fibroblasts through small molecule reprogramming and spheronization, achieving functional osteoblastic materials across all age groups. By primarily targeting the WNT signaling pathway and modularizing small molecules based on their effects on stage-specific genes, we optimized the temporal regulation of small molecules during reprogramming, acquiring a large number of healthy induced osteoblasts (iOBs). These iOBs with traits of functional native osteoblasts are ideal for forming transplantable tissue spheroids. As innovative living materials, the iOB spheroids (iOB-Sps) have demonstrated improved survival, significant self-bone formation, reduced ROS levels in the defect microenvironment, and accelerated endogenous osteogenesis and angiogenesis in vivo, promoting effective healing of bone defects. These material-free iOB-Sps function as self-scaffolding building blocks for biofunctional constructs, offering a promising avenue for clinical autologous bone defect repair, especially for the elderly.

1. Introduction

Bone diseases, have a devastating impact on patients and their families, particularly the elderly, often leading to ill health, disability, a reduced quality of life, and potentially even death [1]. Employing cells as materials precursors offers a promising method for developing living materials with functionalities similar to tissues and the ability for cellular programmability. Osteoblasts are the primary cells responsible for bone formation, producing extracellular matrix proteins and secreting paracrine factors, including VEGF, which regulate endothelial

cell (EC) function. These properties make osteoblasts highly significant for the treatment of bone diseases and the fabrication of living materials that harness the intrinsic biofunctionalities of bone tissue. However, osteoblasts exhibit dysfunction with aging [2], and skeletal stem cells (SSCs) and mesenchymal stem cells (MSCs) that give rise to osteoblasts decrease in quantity and effectiveness over time [3], restricting their available numbers [4]. Moreover, transplanted cells often lack oxygen and nutrients [5], leading to apoptosis and poor long-term survival due to insufficient angiogenesis. This undermines the efficacy of cell-based therapies and increases the risk of rejection and inflammation [6].

Peer review under the responsibility of editorial board of Bioactive Materials.

* Corresponding author.

E-mail address: humin@kmu.edu.cn (M. Hu).

¹ These authors contributed equally.

<https://doi.org/10.1016/j.bioactmat.2025.04.021>

Received 1 November 2024; Received in revised form 14 February 2025; Accepted 16 April 2025

2452-199X/© 2025 The Authors. Publishing services by Elsevier B.V. on behalf of KeAi Communications Co. Ltd. This is an open access article under the CC BY-NC-ND license (<http://creativecommons.org/licenses/by-nc-nd/4.0/>).

Human fibroblasts are a promising source of cells for regenerative medicine due to their reprogrammable nature and high proliferative capacity [7]. Chemically reprogramming is considered a superior reprogramming method over the conventional virus-based reprogramming because of its safety and standardized production [8]. The direct conversion of human fibroblasts into osteoblasts using small molecules has been achieved [8]. However, the applications of these induced osteoblasts in bone tissue engineering and clinical setting for bone defect repair has lagged behind. This is due to several factors. Firstly, the safety profile of the reprogramming process from fibroblasts to osteoblasts still needs to be optimized [9]. Moreover, challenges remain in maintaining the functional activity of reprogrammed cells that do not rely on compounds [10,11]. Additionally, the reprogramming process for bone tissue engineering has yet to be systematically addressed, particularly with regard to low conversion efficiency, immature function of reprogrammed cells, insufficient vascular supply, inadequate nutrient and oxygen delivery within engineered constructs, heterogeneous profiles in individual batches and the inapplicability to cells from elderly person [11–13].

Previously reported chemical reprogramming methods for directly converting fibroblasts into osteoblasts [8,11,14] often result in poor cell survival and limited effects on endogenous cells after engraftment. These reprogrammed cells may not fully replicate the properties of natural osteoblasts *in vivo*, including environmental interpretation, secretion of appropriate extracellular matrix proteins, and support for local angiogenesis, which leads to their dependence on material-based support. These limitations partly stem from identifying small molecules through static endpoint assays based on cell phenotypes and functions, rather than mimicking natural development by leveraging modular combinations of the dynamic behaviors of small molecules to regulate lineage-specific and differentiation-stage-specific gene expression pattern [11]. In the modularized approach, small molecules are selected to maximize coverage of multiple osteogenic development pathways, with a focus on WNT signaling, which is essential for initiating osteogenic lineage commitment and driving the progression into fully differentiated osteoblasts [15]. This strategy may allow for precise combinations of osteogenic signals while minimizing cellular stress.

Here, we present a robust framework for optimizing small molecule combinations to induce complete osteoblastic specification from human fibroblasts while ensuring cell health and spheroid formation of the induced osteoblasts to create living bone repair materials. In the framework, the inclusion of small molecules is based on their ability to activate WNT, as well as their action on other osteogenic pathways. These molecules and their combinations are modularized based on their regulatory coverage of specific-stage genes, including RUNX Family Transcription Factor 2 (RUNX2), Distal-Less Homeobox 5 (DLX5), Sp7 Transcription Factor (SP7), and c-Myc. Three sequential treatment stages are used for complete and precise reprogramming to generate osteoblasts. These iOBs can be stably produced at a large scale from donors of all ages, including the elderly, and exhibit functional traits of young native osteoblasts, which are ideal for forming transplantable tissue spheroids. As innovative living materials, the iOB spheroids have demonstrated improved survival, significant self-bone formation, and the ability to accelerate endogenous osteogenesis and local angiogenesis *in vivo*, enhancing the defect microenvironment for effective bone repair.

2. Results

2.1. Construction of compound modules to transform fibroblasts into osteoblasts

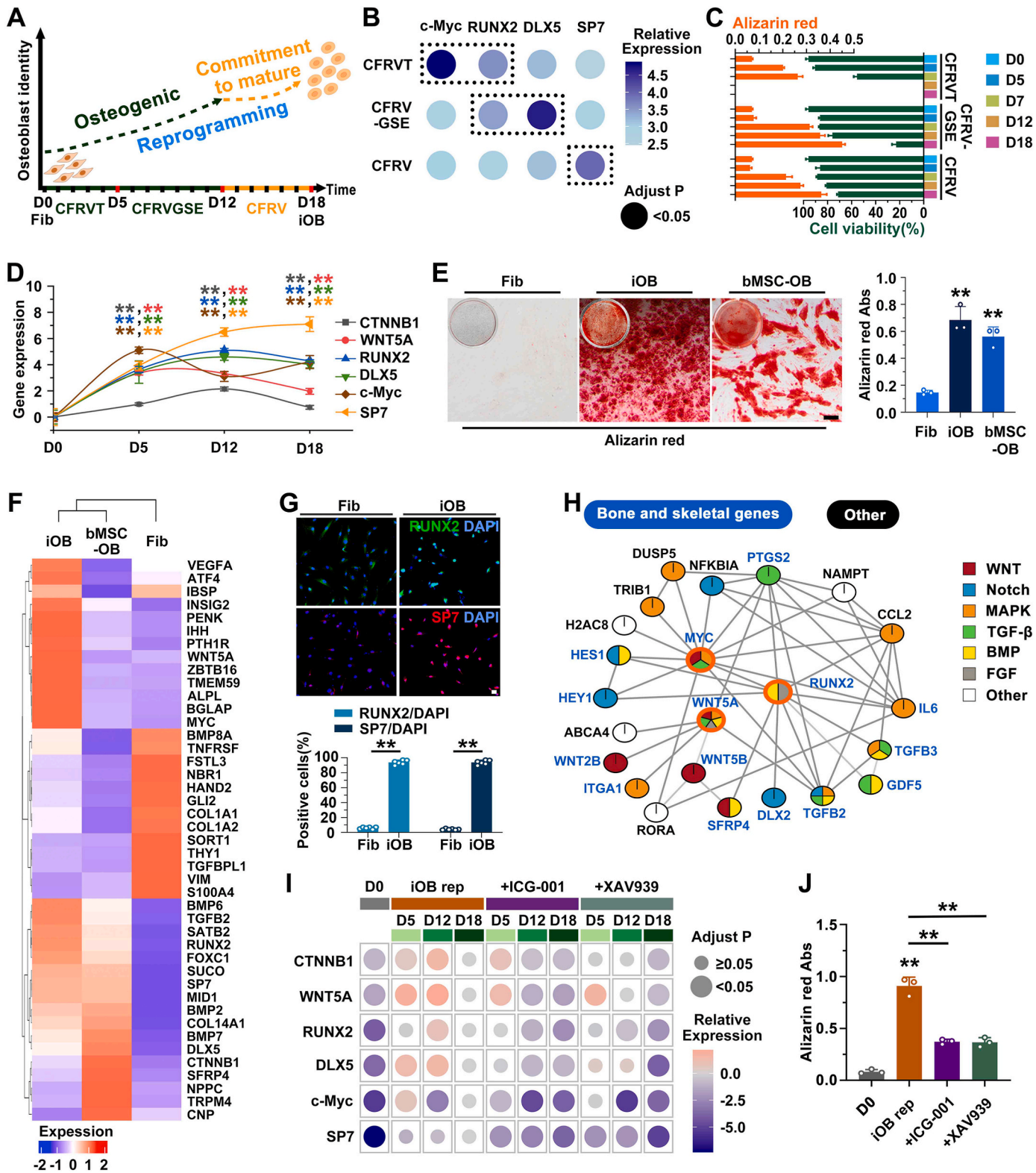
To reprogram human fibroblast into osteoblasts, a modular system was developed that combines small molecules targets with osteogenic development signaling and regulatory network (Fig. 1A; Fig. S1). First, we centered our selection of small molecules on the Wnt/ β -catenin

signaling pathway, which is essential for osteoblast differentiation (Fig. S2A). These compounds were sourced from those that interact with various osteogenic pathways or promote reprogramming while also targeting the WNT pathway (Fig. S2B). Our analysis prioritized compounds that downregulate GSK3 β expression (Fig. S2C). GSK3 inhibitor CHIR99021 (C), adenylyl cyclase activator forskolin (F), TGF- β receptor inhibitor RepSox (R), HDAC inhibitor valproic acid (V) and Trichostatin A (T), PKC inhibitor Go6983 (G), JNK inhibitor SP600125 (S) and DOT1L inhibitor EPZ004777 (E) were identified. Second, we modularized these small molecules and their combinations based on their regulatory coverage of gene expression changes within the osteogenic gene activation network, which includes RUNX2, SP7, DLX5, CTNNB1, and WNT5A, along with the reprogramming factor c-MYC (Figs. S3A–D). The optimized combinations - CFRVT, CFRVGSE, and CFRV - were selected for their effects: CFRVT elicited the highest c-MYC and RUNX2 expression, CFRVGSE induced the highest RUNX2 and DLX5, and CFRV promoted the highest SP7 expression (Fig. 1B; Fig. S3F), all alongside WNT signaling activation (Fig. S3E). Third, exposure to each of these mixtures led to a certain degree of osteogenic conversion in fibroblasts, with each combination exhibiting reprogramming effect at different treatment time points (Fig. 1C; Fig. S4). This conversion was intensified with longer exposure, peaking at 18 days with significant calcium nodule secretion; however, prolonged exposure also increased cell death. Based on the dynamic regulatory capabilities of these combinations on these marker genes, it is recommended to apply them in a sequential order to align with the developmental timeline, ensuring cells acquire the necessary traits and functions. The three small molecule combinations were used in different sequences, where the progressive application of CFRVT, CFRVGSE, and CFRV achieved the highest reprogramming efficiency (Fig. S5A), as it best aligned with the temporal expression of developmental genes. Finally, the stepwise induction program was implemented to convert fibroblasts into osteoblasts (Fig. 1A).

As expected, temporal gene expression analysis showed each treatment stage upregulated different lineage-specific and differentiation-stage-specific genes during the reprogramming (Fig. 1D; Fig. S5B), without affecting cell viability (Fig. S5C). The treated cells adopted mesenchymal morphology with reduced cell size (Fig. S5D) consistent with well-recognized phenomenon in cellular reprogramming [16]. Apparent calcium depositions were observed in iOBs following 14 days in osteogenic medium (Fig. 1E). Global transcriptional changes during the induction were investigated. In hierarchical clustering analysis, we focused on osteoblast-related differentiation and signaling genes, finding that the expression patterns in iOBs resembled those in bone marrow-derived mesenchymal stem cell (bMSC)-derived osteoblasts (bMSC-OB) (Fig. 1F). Two-dimensional principal components analysis (PCA) of cell types according to transcriptome also indicated that iOBs were similar to osteoblasts and distinct from the original fibroblasts (Fig. S7A). RUNX2 and SP7 signals in cell nucleus were observed at the end of the chemical induction (Fig. 1G). Bone sialoprotein II (IBSP) and osteocalcin (OCN) were produced in iOBs cultured in osteogenic medium for 14 days, showing similarities to bMSC-OB (Fig. S6). The nuclear translocation of RUNX2 in treated cells was $96.7\% \pm 1.9\%$, while only $6.0\% \pm 1.8\%$ of untreated fibroblasts exhibited this translocation. Additionally, the proportion of SP7-positive cells in iOBs was $93.7\% \pm 2.9\%$, which, together with RUNX2, indicated a commitment to a mature osteoblast phenotype. In contrast, this proportion in fibroblasts was only $4.4\% \pm 1.1\%$ (Fig. 1G).

2.2. Fibroblasts can be successfully reprogrammed into iOBs via modulation of the WNT signaling pathway with chemicals

To investigate the mechanism of reprogramming to iOBs, we performed KEGG pathway enrichment analysis and Weighted Gene Co-expression Network Analyses (WGCNA) on the transcriptomes of both parental fibroblasts and iOBs (12644 genes). When differentially expressed genes in iOB (Table S5) were functionally annotated using



(caption on next page)

Fig. 1. Construction of compounds regulatory modules and conversion of fibroblasts into iOBs. (A) The strategy for chemical induction of human fibroblasts to osteoblasts. Fib, fibroblast; iOB, induced osteoblast. (B) Gene expression analysis for c-MYC, RUNX2, DLX5 and SP7 after exposure to different individual combinations. Human fibroblasts were treated with CFRVT for 5 days, or with CFRVGSE and CFRV for 7 days respectively. The significance levels were set at $*p < 0.05$ and significance was determined when samples were compared to untreated cells, one-way ANOVA with Bonferroni correction. (C) Temporal cell viability and osteogenic differentiation ability in the fibroblasts exposed to the small molecule combinations for the indicated days. D, day. (D) Temporal gene expression analysis on different treatment stages by RT-qPCR. Gene expression was shown as \log_2 (fold change). Significance was determined when samples were compared to group D0. (E) Alizarin Red staining and Absorbance measurement in fibroblasts, iOBs and bMSC-OB. The fibroblasts, iOBs and bMSCs were cultured in osteogenic medium for 14 days before testing. Significance was determined when samples were compared to Fib group. Scale bar = 100 μm . (F) Heat map and hierarchical clustering analysis of the RNA-seq data showing the genes involved in osteoblast differentiation. (G) Immunofluorescence of RUNX2 and SP7 and the quantification of their expressing cells in fibroblasts or iOBs. The data were presented as means \pm s.d. and $n = 6$ independent experiments in which fibroblasts were derived from six different individuals. Student t-test. $*p < 0.05$, $**p < 0.01$. Scale bar = 50 μm . (H) A network of genes identified by network clustering differently expressed genes in iOBs centered around RUNX2, MYC and WNT5A. The dark edges represented positive correlation of gene expression changes when connected and the light-colored represented negative correlation. The related signaling pathways in osteoblastic commitment were presented in different colors. Gene names were shown in Table S4. (I) Dot plot showed the expression pattern of osteogenic reprogramming related genes in different treated cells. iOB rep represented the cells in the iOB reprogramming process, and the other two groups were cells with ICG-001 or XAV939 added during the reprogramming process. Significance was determined when samples were compared to group iOB-rep D18. The statistical analyses were performed using one-way ANOVA with Bonferroni correction and $n = 3$ independent experiments. The significance levels were set at $*p < 0.05$. (J) Absorbance measurement of Alizarin Red staining of the cells under different treatments presented in I. Significance was determined when samples were compared to group D0 or pairwise comparisons between the groups connected by lines. (D) (E) (J) data were presented as means \pm s.d. and $n = 3$ independent experiments. One-way ANOVA with Bonferroni correction. $*p < 0.05$, $**p < 0.01$.

KEGG pathway analysis (Table S6), the top 15 upregulated and down-regulated pathways were shown, which included osteogenic differentiation pathways and a reduction in fibroblastic growth behavior (Fig. S7B). Several key pathways associated with osteoblast development were also significantly enriched in iOB group, including parathyroid hormone synthesis, secretion and action (PTH), MAPK, WNT and TGF- β signaling pathway (Fig. S7C). These pathways were consistent with the small molecules used during reprogramming.

In the WGCNA analysis, the turquoise, brown, and yellow gene modules showed the strongest correlations in the module-trait relationships (Table S7). The key regulatory genes - WNT5A, c-MYC, and RUNX2 - were identified in these modules respectively, and a network connectivity map was subsequently constructed around them to clarify the direct interactions among the osteogenic pathways and significantly altered genes during reprogramming (Fig. 1H; Table S8). The genes closely associated with RUNX2, MYC and WNT5A were related to skeletal system development, osteoblast differentiation, bone density, bone mineralization, bone remodeling, ossification, skeletal system morphogenesis, angiogenesis, cell cycle and cellular response to stimulus (Fig. S7D). This cluster was enriched for multiple osteogenesis-related signaling pathways, including the involvement of WNT signaling pathway in iOB generation (Fig. 1H).

Given the relevance of the small molecules and RNA-seq findings, we further assessed whether WNT signaling was essential for fibroblast reprogramming into osteoblasts. We used ICG-001 and XAV939, inhibitors of the WNT signaling pathway, in reprogramming cocktails. The addition of these inhibitors resulted in reduced expression of key genes, including CTNNB1, WNT5A, RUNX2, DLX5, MYC, and SP7 (Fig. 1I), along with a significant decrease in osteogenic differentiation capacity (Fig. 1J; Fig. S8). These results indicate that WNT signaling plays a critical role in generating iOBs.

2.3. Chemical reprogramming can efficiently establish functional iOBs from donors of different ages

We applied this protocol to fibroblasts from individuals aged 8, 38, 39, 67, 70, 74, 75, and 79 years to generate induced osteoblasts (iOBs). The protocol proved highly reproducible, resulting in the upregulation of key osteogenic markers - CTNNB1, WNT5A, RUNX2, c-MYC, DLX5, and SP7 - in iOBs derived from fibroblasts of all eight independent donors tested (Fig. S9). All iOBs exhibited significant calcium deposition, as confirmed by Alizarin Red staining (Fig. 2A; Fig. S10A). Importantly, iOBs from individuals aged 67, 70, 74, 75, and 79 demonstrated full osteogenic differentiation potential comparable to that of iOBs and bMSCs from younger individuals. This observation was further supported by the expression of lineage-specific markers, including alkaline phosphatase (ALP), osteocalcin (OCN), Special AT-Rich Sequence-

Binding Protein 2 (SATB2), and Bone Sialoprotein II (IBSP) in iOBs, which were comparable to those in bMSC-OBs from young person (Fig. 2B).

We generated at least 2×10^6 iOBs from an initial population of approximately 1×10^6 fibroblasts in 18 days (Fig. 2C). Starting with a 1 cm^2 skin tissue specimen, we established fibroblast cultures. From passage 1, we obtained 10^6 cells; after expanding to passage 7, we achieved approximately 10^9 cells. Following further expansion, at passage 13 of the fibroblast phase, the cell count reached approximately 10^{11} (Fig. S11A). When fibroblasts at passage 13 were reprogrammed into iOBs, it was possible to generate above 2×10^{11} iOBs from the initial skin sample, regardless of donor age (Fig. 2D). We have established a detailed timeline that correlates the initial fibroblast cell quantity, the corresponding culture duration, and the achievable defect volume that can be repaired by the reprogrammed iOB cells (Fig. S11B).

We also evaluated the ability of iOBs to produce Collagen Type I (COL1) and Vascular Endothelial Growth Factor (VEGF), both critical for bone formation and remodeling. iOBs produced COL1 and VEGF at levels comparable to those observed in bMSC-OBs from young donors (Fig. 2E). Notably, iOBs from older donors, unlike their parental fibroblasts, exhibited a significant increase in COL1 and VEGF production.

Additionally, iOBs from elderly donors did not show signs of senescence. The activity of senescence-associated beta-galactosidase (SA- β -gal) was low in iOBs from both older and younger donors, as well as in bMSC-OBs from younger individuals, whereas it was pronounced in bMSC-OBs from older individuals (Fig. 2F; Fig. S10B). Furthermore, iOBs from elderly donors displayed reduced secretion of IL-6 and lower expression of age-related stress response genes, CDKN1A and CDKN2A, compared to bMSC-OBs from older individuals (Fig. 2G and H).

These findings suggest that this robust three-stage chemical protocol efficiently and reproducibly generates functional iOBs from young and elderly individuals.

2.4. The iOBs gained advanced functions via spheronization

Cell 3D spheroids have shown improved “therapeutic signaling”, as well as enhanced homing and survival capabilities following in vivo transplantation [17]. High-quality cells were required to ensure robust spheroid formation and functionality. We characterized their properties to investigate the potential of iOB spheroids (iOB-Sp) for bone regeneration and tissue engineering. iOBs were aggregated via centrifugation, using cell numbers ranging from 7×10^4 to 2×10^6 (Fig. 3A). The size of the resulting spheroids varied from 1 mm to 3 mm in diameter, depending on the cell counts (Fig. 3B). After spheroid formation, the cells maintained good viability (Fig. S12). iOBs cultured in a monolayer could form spheroids effectively. Upon dissociation and replating, the cells displayed stable viability and numbers (Fig. 3C).

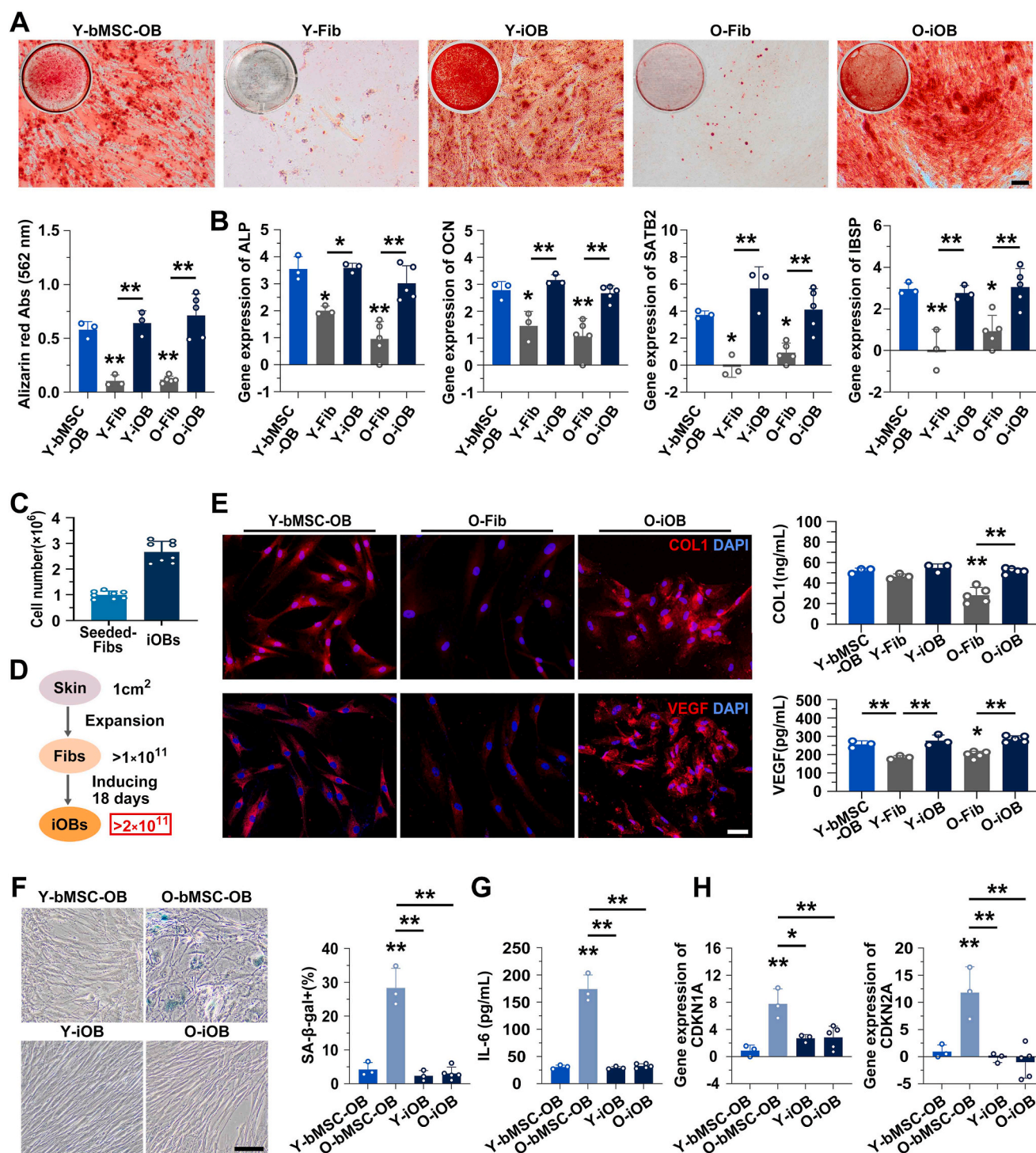


Fig. 2. Characteristics of iOBs derived from donors with different ages. (A) Alizarin Red staining of osteoblasts derived from bMSCs (31 years), iOBs from 8-, 79-year-old donors and their parent fibroblasts after cultured in osteogenic medium for 14 days. $n \geq 3$ independent experiments. Y, young referred to individuals under 65 years of age; O, old referred to individuals aged 65 years and older. Scale bar = 100 μ m. (B) mRNA levels for ALP, OCN, SATB2 and IBSP after 14 days culture in osteogenic medium. The Y-bMSC were isolated from donors of 26-,31-,33-year-old. The Y-Fib or Y-iOBs were derived from donors of 8-,38-,39-year-old. The O-Fib or O-iOBs were derived from donors of 67-,70-,74-,75-,79-year-old. Gene expression was shown as \log_2 (fold change). $n \geq 3$ independent experiments. (C) Cell number of starting fibroblasts and resultant iOBs after 18 days' treating. $n = 8$ individuals' iOBs. (D) Schema for extent of cell expansion during iOBs conversion from skin fibroblasts. (E) The secretion of COL1 and VEGF in Y-bMSC-OB, iOBs and their parent fibroblasts. Y-bMSC-OBs in immunofluorescence images were derived from 31-year-old donors, and O-iOBs and its parent O-Fib were from 79-year-old donor. $n \geq 3$ independent experiments. Scale bar = 50 μ m. (F) SA- β -gal activity in Y-bMSC-OB, O-bMSC-OB, Y-iOB from a 39-year-old individual, O-iOB from a 79-year-old donor. $n \geq 3$ independent experiments. Scale bar = 100 μ m. (G) The secretion of IL-6 in Y-bMSC-OB, O-bMSC-OB, Y-iOBs and O-iOBs. $n \geq 3$ independent experiments. (H) mRNA levels for CDKN1A and CDKN2A in osteoblasts derived from bMSCs and iOBs from young or old individuals. Gene expression was shown as \log_2 (fold change). $n \geq 3$ independent experiments. (A) (B) (E) (F) (G) (H) data were presented as means \pm s.d. Significance was determined when samples were compared to Y-bMSC-OB or pairwise comparisons between the groups connected by lines. One-way ANOVA with Bonferroni correction. $*p < 0.05$, $**p < 0.01$.

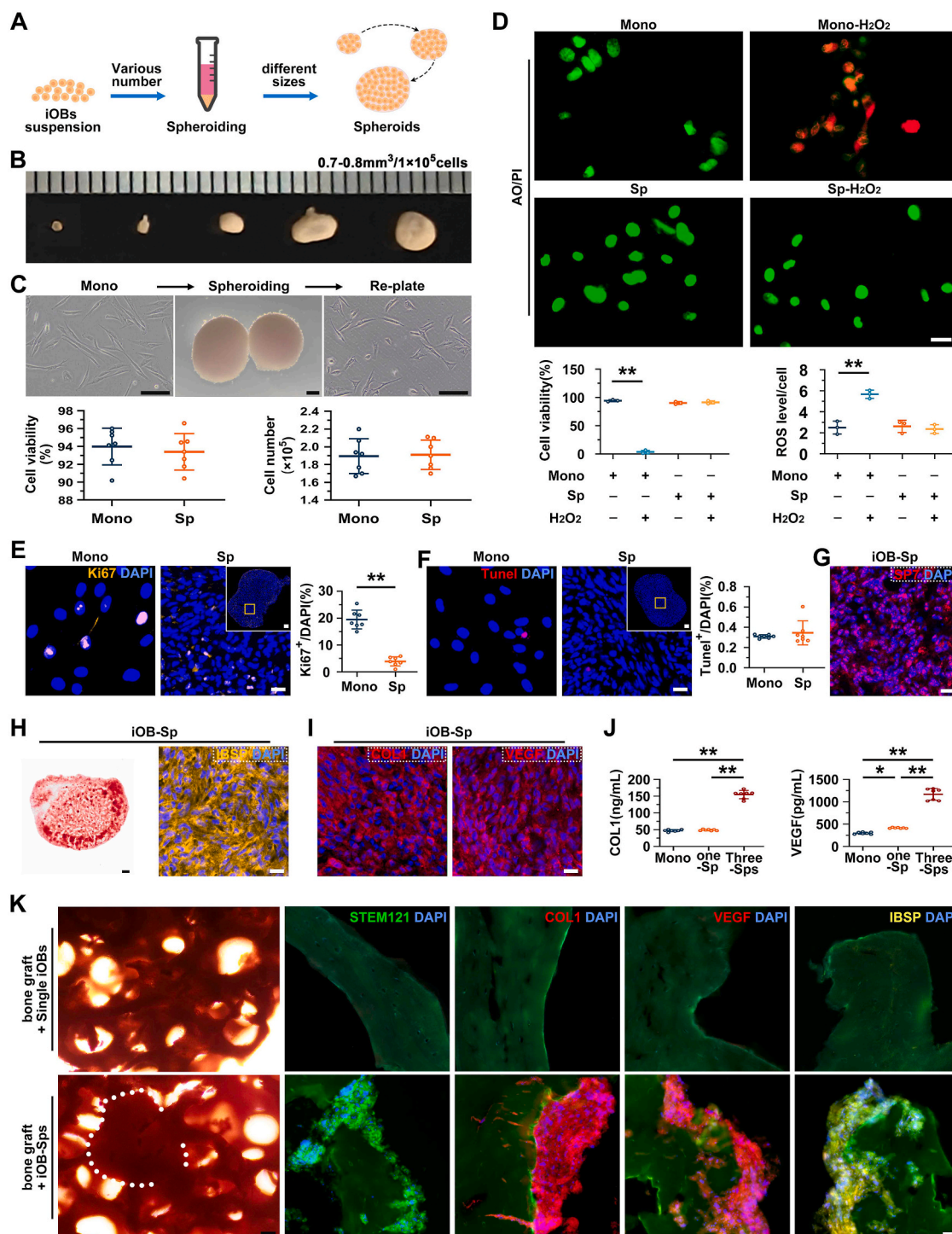


Fig. 3. Generation and characteristics of iOB spheroids (A) Gravitational forced aggregation method to generate iOB-Sps (B) iOB-Sps at different sizes with various numbers of cells. About 1×10^5 iOBs could be used to prepare a spheroid with the volume of 0.7–0.8 mm³. (C) Analysis of cell viability following the formation of cell spheroids. $n = 7$ independent experiments. Student t-test. $*p < 0.05$, $**p < 0.01$. Scale bar = 200 μ m. (D) Analysis of cell activity when iOBs were exposed to H₂O₂ in monolayer cultures or in spheroids. The viability of cells was detected by AO/PI assay. The ROS levels were detected by DCFH-DA. $n = 3$ independent experiments. Scale bar = 20 μ m. (E)–(F) Immunofluorescent staining of Ki67 or TUNEL in monolayer cultures and in spheroids. The data were presented as means \pm s.d., Significance was determined when samples were compared to monolayer-cultured cells. Student t-test. Scale bar = 100 μ m in the whole spheroid images. Scale bar = 20 μ m in the magnified images. (G) Immunofluorescent staining of SP7 in spheroids. Scale bar = 20 μ m. (H) Alizarin red staining and IBSP immunofluorescent staining of iOB-Sps cultured in osteogenic medium for 14 days. Scale bar = 100 μ m (Left); Scale bar = 20 μ m (Right). (I) Immunofluorescent staining of COL1 and VEGF in spheroids. Scale bar = 20 μ m. (J) Quantification of COL1 and VEGF secretions from 2×10^5 monolayered iOBs, one spheroid with 2×10^5 cells, and three spheroids with 2×10^5 cells per spheroid. All of them were cultured in the same volume. (K) The adhesion of iOBs with decellularized porcine cancellous bone. The embedded iOBs were in single cell suspension or in 3D spheroid. Optical microscopic pictures, STEM121 (green), COL1 (red), VEGF (red), IBSP (yellow-gold), and DAPI (blue) nuclear staining were shown. Mineralized bone matrix was shown by green fluorescence. Scale bar = 200 μ m in optical microscopic pictures. Scale bar = 20 μ m in fluorescence images. (D)–(J) data were presented as means \pm s.d., Significance was determined when samples were compared to monolayer-cultured cells or pairwise comparisons between the groups connected by lines. One-way ANOVA with Bonferroni correction. $*p < 0.05$, $**p < 0.01$.

Compared to iOB, iOB-Sp demonstrated improved differentiation into mature osteoblasts, elevated anti-ROS factors, such as NRF2 and catalase expression (Fig. S13) and increased secretion levels of VEGF (Fig. S13). Given that hypoxia in bone defects can induce excessive reactive oxygen species (ROS) production, which is detrimental to cell viability, we evaluated the impact of spheroidal formation on the cells resistance to ROS. Compared to monolayer cultures, iOB spheroids

exposed to H_2O_2 demonstrated improved resilience, showing no significant increase in ROS production and no decline in cell viability (Fig. 3D). This suggests that the spheroid structure enhances the cells' ability to manage oxidative stress and protect against cell death. After being stressed and replated, the iOBs retained healthy morphology similar to those of 2D-cultured iOBs under normal conditions (Fig. S14A).

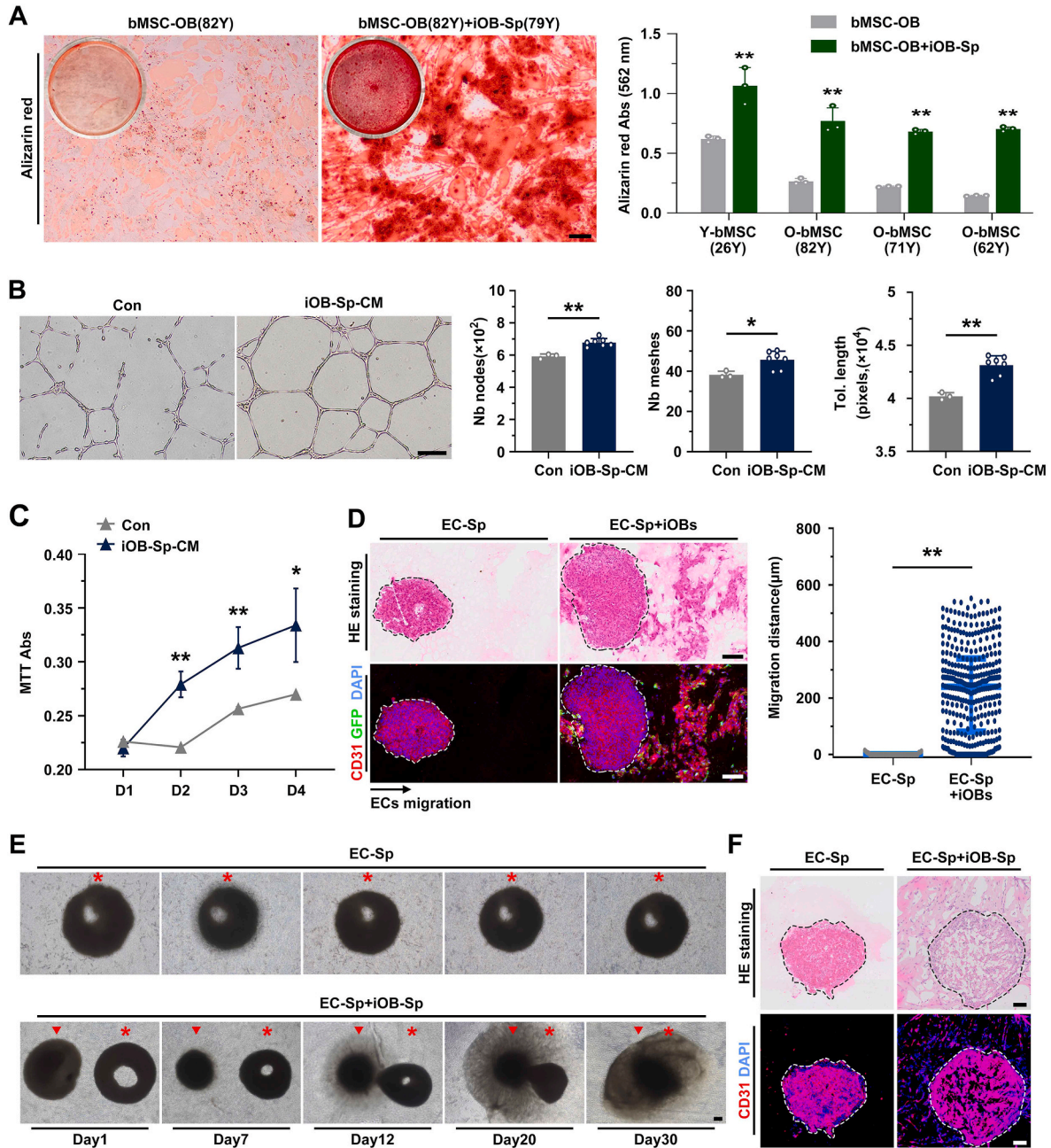


Fig. 4. Contribution of iOB-Sps to endogenous bMSCs and endothelial cells in vitro (A) Analysis for the osteogenic differentiation capability of bMSCs from 26-, 62-, 71-, 82-year-old individuals when co-cultured with O-iOB-Sps. Osteoblasts derived from bMSCs of a 82-year-old individual were shown in the alizarin red staining image. Scale bar = 100 μm . (B) A cord formation assay and quantification of tube formation for the endothelial cells under normal cultures or conditional medium (CM) of iOB-Sps pretreatment. Nb.nodes, number of nodes; Nb.meshes, number of meshes; Tol.length, total length. Scale bar = 200 μm . (C) MTT assay showing the proliferation of endothelial cells in iOB-Sps pretreated group and in untreated control group. $n = 3$ independent experiments in control group, $n = 7$ in iOB-Sp-CM group. (D) The endothelial cell migration from EC spheroid (EC-Sp) in contact-based model with iOBs. $n = 3$ independent experiments. $n = 47$ cells migrating outside the dashed boundary of the spheroid in EC-Sp group, $n = 349$ cells in EC-Sp + iOBs group. The sections of EC spheroid were stained with H&E (Upper) or CD31 antibody (Lower). Scale bar = 100 μm . (E) The endothelial cell migration in non-contact-based model with iOB-Sps over time. As a control, EC spheroid was placed within Matrigel without iOB-Sp (the upper image). Triangle indicated iOB-Sp; Asterisk, EC spheroid. Scale bar = 200 μm . (F) Analysis of the EC migration from its spheroid using H&E (Upper) staining and CD31 (Lower) immunofluorescence staining. Scale bar = 100 μm . (A)–(D) data were presented as means \pm s.d. Student t-test. * $p < 0.05$, ** $p < 0.01$.

iOBs in 3D cultures exhibited reduced Ki67 positivity, indicating lower proliferation activity compared to cells in monolayer culture (Fig. 3E). However, apoptosis did not increase in the spheroids (Fig. 3F). Notably, more than 90 % of the cells in spheroids remained SP7-positive, indicating that the iOBs in 3D culture were committed to mature osteoblast differentiation (Fig. 3G). When iOB spheroids were cultured in osteogenic medium for 14 days, they exhibited significant calcium deposition and production of IBSP (Fig. 3H).

Furthermore, iOB spheroids continued to express COL1 and VEGF (Fig. 3I). Under the same culture conditions and with an equivalent cell number, iOB spheroids and monolayer cultures secreted similar amounts of COL1. However, iOB spheroids secreted significantly more VEGF (Fig. 3J). Additionally, 3D spheroids supported a higher number of iOBs compared to monolayer cultures within the same culture volume, leading to increased production of COL1 and VEGF. This enhanced secretion in spheroids created a more favorable microenvironment for bone formation by concentrating these signals in a confined space.

In a separate experiment, we cultured both iOB single cells and iOB spheroids with decellularized porcine cancellous bone (Fig. S14B) for 5 days. The iOB single cells did not adhere to the bone tissue and failed to remain viable (Fig. 3K; Fig. S14C). In contrast, iOB spheroids successfully integrated with the decellularized bone, secreting COL1 and VEGF while differentiating into mature osteoblasts (Fig. 3K; Figs. S14D–G). These results suggest that iOB spheroids possess significant biological activity, providing nutrients and a supportive matrix for cell survival, migration, and lineage-specific differentiation. This reduces the need for additional active substances from other biomaterials.

2.5. Enhancing endogenous cells functions when co-cultured with iOB-Sps *in vitro*

bMSCs and endothelial cells (ECs) play crucial roles in bone repair, as bMSCs differentiate into osteoblasts, while ECs contribute to vascularization. However, aged bMSCs have a diminished capacity for osteogenic differentiation. We established a transwell system to co-culture iOB spheroids (iOB-Sp) and bMSCs, in which iOB-Sp in the upper inserts cannot migrate through the Transwell membrane to the lower chamber (Fig. S15). When aged bMSCs were co-cultured with iOB-Sp derived from old donors in a transwell insert, aged bMSCs displayed significantly enhanced osteogenic differentiation (Fig. 4A; Fig. S16).

Human umbilical vein endothelial cells (ECs) were cultured in a conditioned medium from iOB-Sps for 24 h and replated on growth factor-reduced Matrigel. Cord networks formed in both iOB-Sp treated and untreated groups by day 1, but the treated group exhibited thicker cords, more branching, and more significant cell clustering at branch points (Fig. 4B). Quantitative analysis confirmed that iOB-Sps promoted cord network formation, as evidenced by an increase in branch nodes, meshes, and total cord length (Fig. 4B). Additionally, ECs proliferation was enhanced when treated with conditioned medium from iOB-Sps for 24 h (Fig. 4C).

To further investigate the effect of iOB-Sps on EC migration, we created EC spheroids using the hanging drop method and developed two co-culture models within 3D spheroid microenvironments based on growth factor-reduced Matrigel: a contact-based model and a non-contact-based model. In the contact-based model, an EC spheroid was embedded within Matrigel containing uniformly distributed iOB single cells. As a control, an EC spheroid was cultured in Matrigel alone. By day 3 of co-culture, ECs in the iOBs co-culture exhibited significant migration away from the spheroid, whereas almost no migration was observed in the control group (Fig. 4D).

In the non-contact-based model, toroid-shaped EC spheroid and iOB-Sp were co-cultured within the same Matrigel sphere with a 400 μ m gap between them. Over 30 days, the EC spheroid progressively migrated toward the iOB-Sp (Fig. 4E). Analysis of frozen sections of the EC spheroid revealed that ECs had dispersed from their original spheroid structure (Fig. 4F).

2.6. The iOB-Sps showed high survival and function for transplantation on a murine femoral defect model

To evaluate the therapeutic potential of iOB spheroids (iOB-Sps), we utilized a femoral defect model in NOD/SCID mice with a defect volume of approximately 4 mm³ (Fig. 5A). The iOB-Sps were tailored to match the size of the injury site, with approximately 1.3×10^5 iOBs forming a spheroid of 0.9–1 mm³ in volume (Fig. 5B). Four iOB-Sps, derived from a 79-year-old donor, were transplanted into the injury site to fill the defect (Fig. 5C). As controls, bMSCs from a 31-year-old donor and fibroblasts from the same donor as the iOB-Sps were transplanted into similar defects, with bMSCs and fibroblasts delivered as single-cell suspensions mixed with Matrigel, or fibroblasts transplanted in the form of spheroids (Fib-Sps). After 28 days, microCT imaging revealed that the injury sites treated with iOB-Sps were covered with bridging calluses, comparable to those seen in bMSC-transplanted femurs. In contrast, fibroblast or Fib-sp-treated sites showed no evident bone repair (Fig. 5D; Fig. S17). The results in the Fib-sp transplantation group showed that bone defects were not restored merely by the presence of a cell scaffold formed by fibroblasts, and the model did not facilitate bone defect repair solely through spatial filling or bridging by the scaffold material. The repair outcomes were further quantified using bone volume (BV)/total volume (TV), bone surface (BS)/total volume (TV), trabecular number (Tb. N), and bone mineral density (BMD) measurements (Fig. 5E). These data demonstrated that iOB-Sps from elderly donors exhibited bone repair capabilities similar to those of younger bMSCs.

To assess bone matrix production by the grafted cells, Hoechst 33342-labeled cells were transplanted into the defect site. A large number of blue fluorescently labeled nuclei from iOBs and bMSCs were observed in the callus under UV light. Consistently, H&E staining showed parallel collagen bundles forming lamellar structures in the new bone tissue. Under polarized and ultraviolet light, the stained tissues revealed a highly mineralized new bone matrix (Fig. S18). No abnormal tissue growth was observed around the regenerated area, indicating no tumor formation from the transplanted iOB-Sps. Correspondingly, Safranin/Fast Green staining confirmed the complete maturation of iOB-Sp transplants into calcified bone, while Alizarin Red staining verified ossification at the callus of the iOB-transplanted femurs (Fig. S19). These results indicate that the local transplantation of iOB-Sps accelerated bone healing at defect sites.

To further assess the survival and differentiation of the transplanted iOB spheroids, we used iOB-Sps transduced with LV-EGFP and implanted them into the defects. At day 28 post-transplantation, the number of TUNEL+/GFP+ cells in the grafts was very low, similar to those *in vitro* cultured iOB-Sps before transplantation (Fig. 5F), indicating high cell viability. In addition, no expression of the cell proliferation marker Ki67 was detected in the transplanted iOBs (Fig. 5G), which may contribute to the safety of the grafted cells. GFP+ cell counts showed no significant change in the number of iOBs 28 days after transplantation (Fig. 5H), indicating the cells were surviving well. Elevated ROS levels in the bone defect area can harm the survival of transplanted cells. However, the transplanted iOB-Sps not only maintained cell viability in the stressed microenvironment but also improved the local microenvironment of the bone defect by reducing ROS levels (Fig. S20). Approximately 80 % of GFP+ cells expressed IBSP (Fig. 5I; Figs. S21A and B), suggesting that the grafted iOBs successfully differentiated into mature osteoblasts. Immunohistochemical staining for OCN, a late-stage bone matrix protein, revealed intense signals in the newly formed matrix, indicating greater secretion of mature bone matrix protein by the iOB-Sps (Fig. S21C).

Furthermore, iOBs did not form tumors. In a 180-day study, no tumor formation was observed in NOD/SCID mice transplanted with iOBs (Fig. S22) which show the high safety of iOBs for administration *in vivo*.

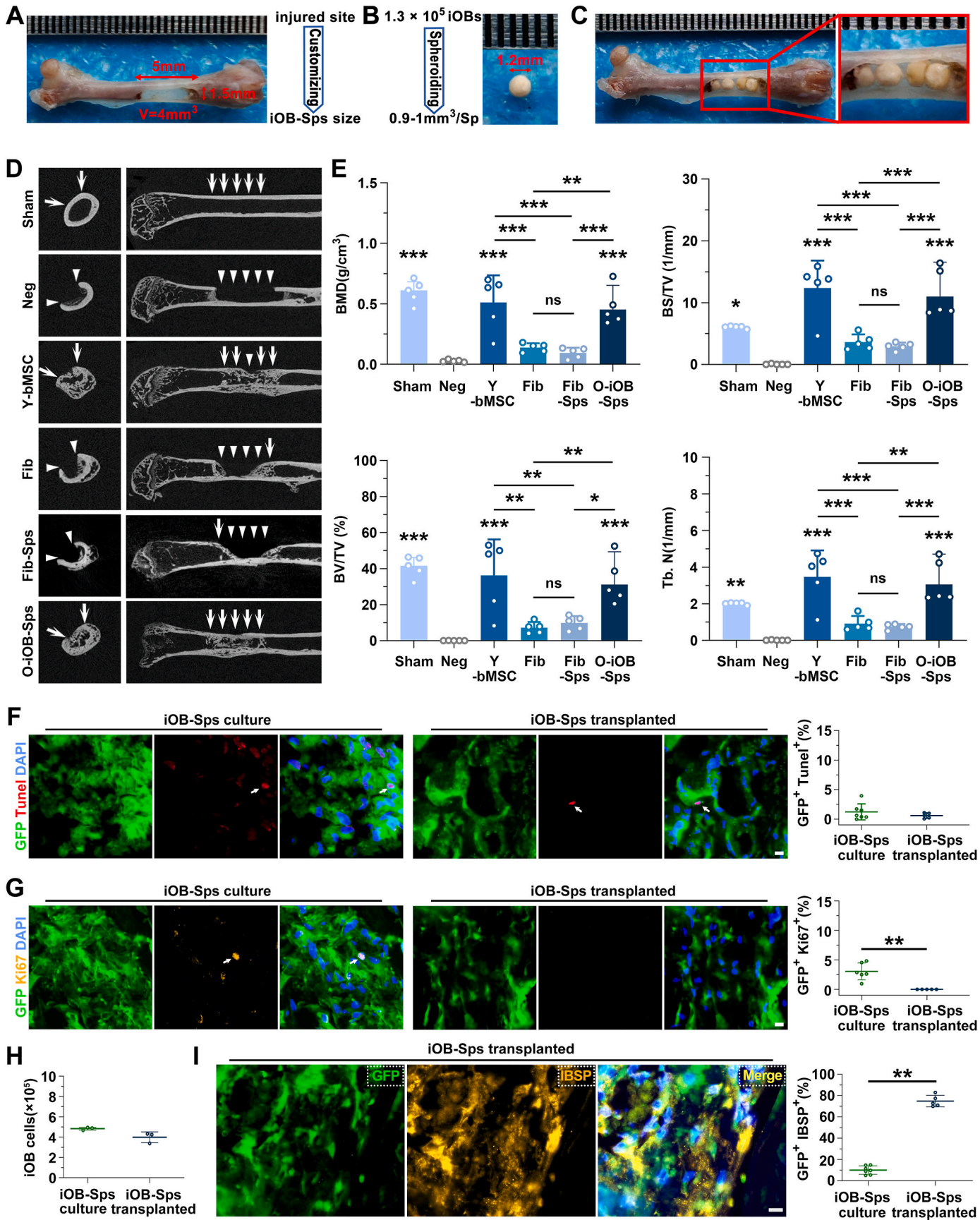


Fig. 5. Therapeutic effects of iOB-Sps on bone regeneration (A) 5 mm in the length and 1.5 mm in width femoral bone defect was created by dental drill on the right femur. Each scale of the ruler indicates 0.5 mm. (B) The preparation of iOB-Sps to fit the damaged size. (C) The transplantation of iOB-Sps into bone defect. (D) μ CT imaging of the femur transplanted by Fibs, Fib-Sps, bMSCs and iOB-Sps in NOD/SCID mice with femur defect. iOB-Sps were derived from old donors, O = Old. (E) BMD, BS/TV, BV/TV, Tb. N values in bone defect healing. $n = 5$ independent experiments. Significance was determined when samples were compared to group Neg or pairwise comparisons between the groups connected by lines. (F) Analysis of TUNEL staining for iOBs apoptosis in spheroid before and after 28-days transplantation. $n = 7$ independent experiments in iOB-Sps culture in vitro and $n = 5$ independent experiments in iOB-Sps transplanted in vivo. (G) Analysis of Ki67 fluorescent staining for iOBs proliferation in spheroid before and after 28-days transplantation. $n = 7$ independent experiments in iOB-Sps culture in vitro and $n = 5$ independent experiments in iOB-Sps transplanted in vivo. (H) Counting of iOBs when cultured in vitro spheroid and in vivo post transplantation. (I) Representative images and quantification analysis of GFP and IBSP positive cells in bone defects. $n = 7$ independent experiments in iOB-Sps culture in vitro and $n = 5$ independent experiments in iOB-Sps transplanted in vivo. (E)–(I) data were presented as means \pm s.d. * $p < 0.05$, ** $p < 0.01$, *** $p < 0.001$. One-way ANOVA with Bonferroni correction in (E); Student t-test in (F)–(I). Scale bar = 10 μ m in (F) (G) (I).

2.7. Transplantation of iOB-Sps can enhance endogenous osteogenesis and angiogenesis in vivo on a murine femoral defect model

We conducted a series of examinations to evaluate the contribution of iOB-Sps transplants to the bone healing process. Immunohistochemical analysis using a COL1 antibody revealed significantly higher COL1 production in the iOB-Sps engrafted group compared to the untreated control group (Fig. 6A and D). Post-transplantation, elevated COL1 secretion was detected both in and around the transplanted iOBs (Fig. S23), indicating that iOBs not only produced COL1 themselves but also stimulated endogenous cells to increase COL1 secretion. In addition, a substantial amount of bone matrix protein, IBSP, was observed at the defect site (Fig. 6B, C and 6E), further demonstrating that the transplanted cells promoted the healing process and bone regrowth. IBSP signals were detected within and surrounding the engrafted cells (Figs. S21A and B), suggesting that iOB-Sps enhanced endogenous osteogenic activity.

In parallel, we observed increased VEGF secretion in the iOB-Sps treated group (Fig. 7A). The number of VEGF-positive cells in the callus of the iOB-Sps group was higher (Fig. 7D), with VEGF signals detected both within and around the transplanted iOBs (Fig. S24). This indicates that the exogenous iOBs not only secreted VEGF but also stimulated endogenous cells to produce the protein. Correspondingly, effective angiogenesis, marked by CD31 expression, was observed in the iOB-Sps group (Fig. 7B, C and 7E), indicating that iOBs induced endogenous revascularization. To demonstrate the abundant secretion of VEGF by iOB-sp cells in vivo, we performed IHC staining on the iOB-Sp transplant group, co-staining with a human-specific anti-VEGF antibody and a mouse-specific anti-CD31 antibody. The result showed the defect repair area still exhibited obvious VEGF secretion by iOB cells (GFP+), with a marked accumulation of endogenous vascular endothelial cells (CD31⁺) surrounding them at 28 days post-transplantation (Fig. S25).

To explore the mechanism of iOB-Sps in treating bone defect, we further analyzed the in vivo expression of the angiogenesis-related factor VEGF, osteoblast maturation marker osteocalcin (OCN), and antioxidant-related protein NRF2 at the single-cell level in tissue sections of the transplanted iOB-sp compared to the control group (bMSC-sp/Fib-sp) post 7 days transplantation. The results showed that iOBs highly secreted VEGF and activated endogenous ECs, which could enhance angiogenesis at the defect site (Fig. S26). iOBs also exhibited mature osteoblastic functionality by releasing high levels of osteocalcin, which contributed to the upregulation of antioxidant proteins. Additionally, iOB-Sp expressed high levels of the antioxidant protein NRF2. Correspondingly, iOB-Sp significantly reduced ROS levels in the bone defect microenvironment (Fig. S27). The ability of iOB-Sp to promote angiogenesis and reduce ROS production was stronger than that of fibroblast and bMSC.

These results revealed that iOB-Sps could improve the niche in bone repair by increasing the necessary signals such as COL1, IBSP or VEGF to induce eventual bone matrix formation and vascularization to develop new bone.

3. Discussion

Here, we present a chemical reprogramming method to generate highly functional osteoblasts and their spheroids from human fibroblasts of all ages. These cells have been shown to be effective in repairing bone defects and exhibit excellent safety profiles. The approach can generate enough iOBs to customize cell spheroids tailored for various sizes of bone defects (Fig. 8). Such cell conversion efficiency enables the customized modular bottom-up assembly of multiscale constructs using living cells and lays a foundation for the clinical treatment of bone diseases.

RUNX2 expression defines cells at a preosteoblast stage and subsequent SP7 expression defines the cells' differentiation to osteoblasts [18]. The expression of RUNX2 and SP7 marks the commitment to a mature osteoblast. DLX5, in conjunction with RUNX2, osteocalcin, and alkaline phosphatase, aids preosteoblast to osteoblast transition [19]. MYC and RUNX2 together initiate reprogramming toward the osteoblast lineage [20].

In the first stage, the CFRVT combination elevates RUNX2 and MYC to initiate osteogenic reprogramming. In the second stage, Trichostatin A was removed to avoid its long-term cell cytotoxicity and replaced with GES, boosting RUNX2, DLX5, and SP7 to promote osteoblastic differentiation. In the third stage, only CFRV is used to further increase RUNX2 and SP7, maximizing osteoblast conversion while reducing cellular stress (Fig. 1D; Figs. S4 and S5). This time-sequenced treatment of chemical combinations established a network driving complete osteoblastic specification centered on RUNX2, MYC, and WNT5A, featuring significantly altered genes associated with osteogenic differentiation and maturation (Fig. 1H). Despite these promising findings, a more comprehensive understanding of the molecular targets and their underlying mechanisms, as well as epigenetic modulation is required through further systematic research.

This tiered modular approach can obtain iOBs from people with all ages, especially for elderly and maintain cell viability in the stress-ridden bone defect environment, including high ROS levels from hypoxia, nutrient deficiency, apoptosis signaling, and bone matrix disruption. Unlike previously reported induced osteoblasts, these cells exhibit mature functionality and efficient self-bone formation in vivo and produce type I collagen, osteocalcin, IBSP, and VEGF to facilitate bone healing without the need for additional osteoinductive molecules (Figs. 5–7), while ensuring safety without tumorigenicity (Fig. S22) and bypassing an intermediate pluripotent stage.

The use of cell-rich living materials with native intrinsic bio-functionalities to restore damaged tissue is one of the major goals of tissue engineering. Cells possess unique living attributes that are beyond the reach of current synthetic and semi-synthetic biomaterials [21]. However, previously reported osteoblasts generated in vitro [8,22], still rely on additional scaffolds like Matrigel, COL1 sponges or nanofiber for cell survival and to direct osteogenic differentiation in vivo, which are limited by the scaffold type and do not fully replicate life-like properties, such as environmental sensing and response. In this study, iOB spheroids serve as building blocks, enabling high cell mass and bone formation in defects. Unlike traditional methods that rely on materials like Matrigel or hydrogel, these spheroids boost cell survival without external

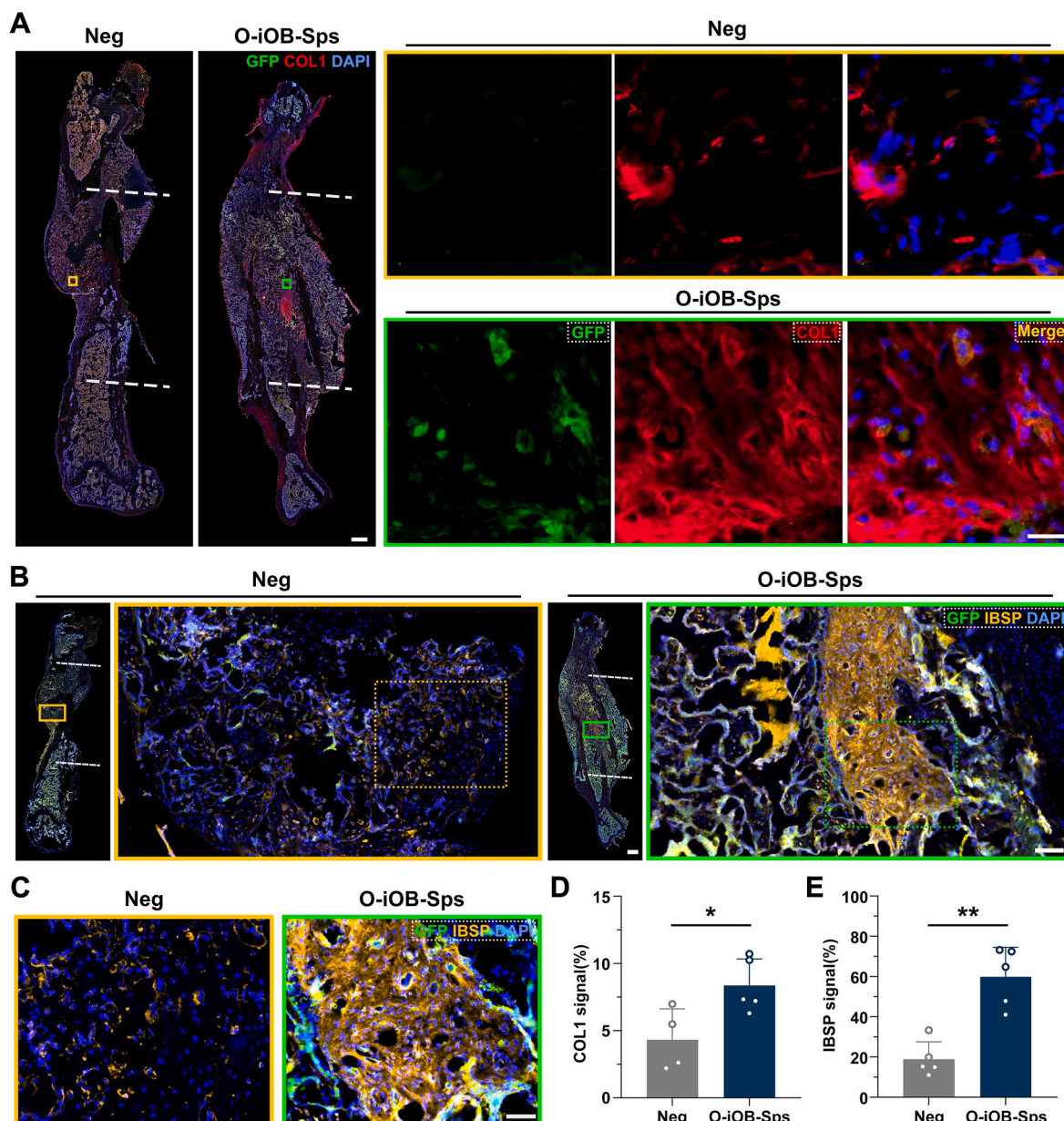


Fig. 6. Enhancement of endogenous osteogenesis induced by iOB-Sps

Biopsies were obtained 4 weeks after iOB-Sps transplantation into mouse femur defects. DAPI nuclear counterstain as indicated in blue, iOB-labeled GFP counterstain as indicated in green.

(A) Regeneration of damaged sites shown in a panoramic view of the complete femur and in high-resolution image stained for COL1 (red). Scale bar = 500 μ m in complete femur images; Scale bar = 10 μ m in high-resolution images.

(B) Regeneration of damaged sites shown stained for IBSP (yellow gold). Scale bar = 500 μ m in complete femur images; Scale bar = 100 μ m in high-resolution images.

(C) Magnification of IBSP staining of the boxed area shown in (B). Scale bar = 50 μ m.

(D) The proportion of COL1 positive area in the total defective area. $n = 4$ independent experiments in untreated negative group and $n = 5$ independent experiments in iOB-Sps treatment group.

(E) The proportion of IBSP positive area in the total defective area. $n = 5$ independent experiments.

(D) (E) data were presented as means \pm s.d. Student t-test. * $p < 0.05$, ** $p < 0.01$.

support. They thrive in harsh conditions and function collectively to influence endogenous cells.

Our results suggest that iOB-Sp is more resistant to ROS production and maintains better viability than monolayer iOBs, and they also effectively reduce ROS levels in the bone defect environment. We believe this is due to a combination of internal and external factors. Internally, when iOBs form spheroids using methods like v-bottom plates or hanging drop, they behave similarly to mesenchymal stem cells (MSCs) in 3D cultures exhibiting reduced metabolic activity and

proliferation [23], which leads to a kind of protective, quiescent state [24]. In this state, the cells consume less ATP in their mitochondria [25], making them less vulnerable to ROS-induced damage. Externally, the formation of spheroids promotes tighter cell-cell interactions through gap junctions [26], creating a barrier that limits chemical exchange. This barrier helps establish a microenvironment that is conducive to reducing the exposure of cells in the spheroid to harmful chemicals, thereby limiting ROS penetration and protecting the cells. Furthermore, the spheroid formation process upregulates antioxidant proteins such as

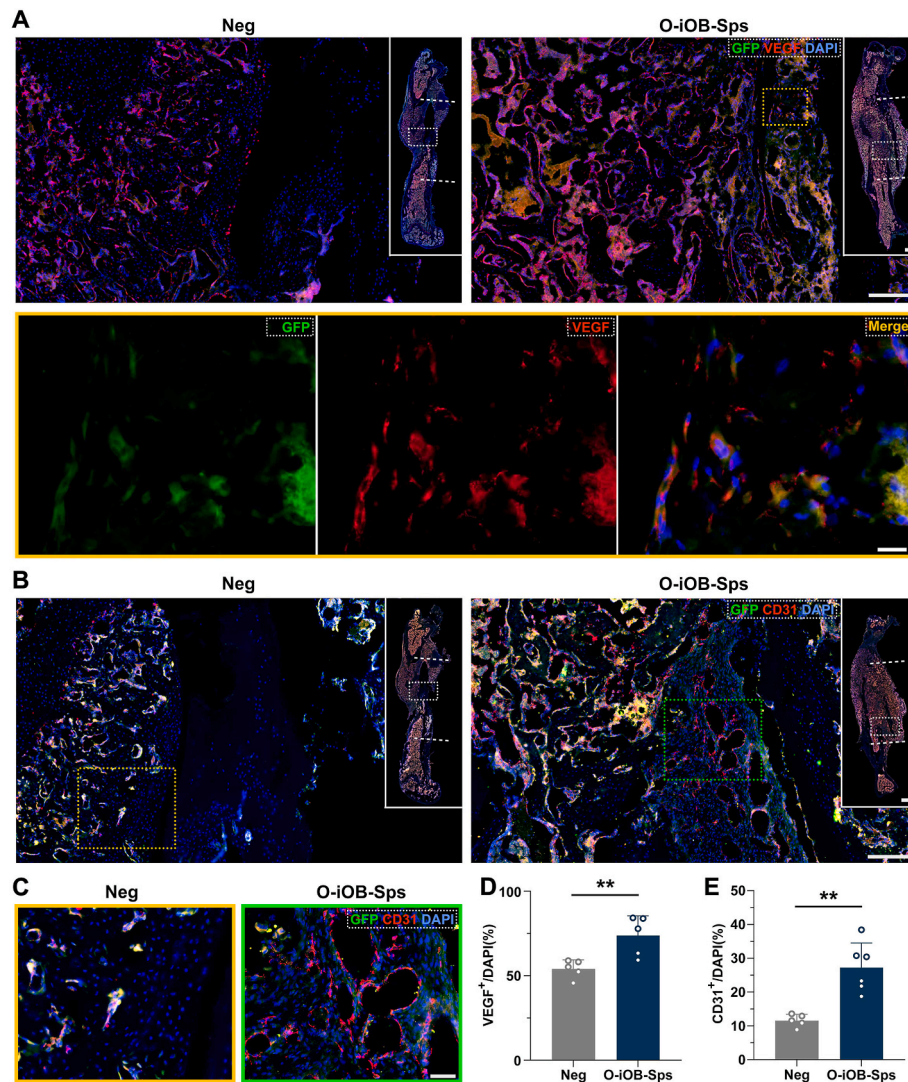


Fig. 7. Revascularization in defective lesion mediated by iOB-Sps

DAPI nuclear counterstain as indicated in blue, iOB-labeled GFP counterstain as indicated in green.

(A) Immunohistochemical staining of VEGF (red) in damaged sites shown at whole mouse femur and at high resolution. The boxed area in the upper image was shown in high magnification on the lower. Scale bar = 500 μ m in complete femur images; Scale bar = 200 μ m in high-resolution images (Upper), Scale bar = 20 μ m in high-resolution images (Lower). (B) Immunohistochemical staining of CD31 (red) in damaged sites. Scale bar = 500 μ m in complete femur images; Scale bar = 200 μ m in high-resolution images. (C) Magnification of CD31 staining of the boxed area shown in (B). Scale bar = 50 μ m. (D) The percentage of VEGF positive cells in defective area. n = 5 independent experiments. (E) The percentage of CD31 positive cells in the defective area. (D) (E) data were presented as means \pm s.d. Student t-test. * p < 0.05, ** p < 0.01.

NRF2 and catalase, as well as Osteocalcin, which can upregulate antioxidant proteins [27], effectively reducing ROS levels in vitro and in vivo. Together, these factors likely contribute to the enhanced resilience of iOB-Sp compared to the 2D monolayer cells.

In this study, we also demonstrated that the three-dimensional (3D) spheroid formation of iOB (iOB-sp) markedly enhances its paracrine and nutritional effects compared to conventional two-dimensional (2D) monolayer cultures [26]. Consistent with previous reports on mesenchymal stem cells (MSCs) cultured in 3D conditions, iOB-sp secreted significantly higher levels of VEGF (Fig. 3J) and matrix proteins, attributable to the formation of a pure-cell 3D scaffold that supports a more significant number of functional iOB cells. This scaffold facilitates cell survival and function (Fig. 3K; Fig. 5F), ensuring an adequate supply of active osteoblasts in the bone defect microenvironment to protect endogenous cells and provide a supportive matrix for cell migration and survival through paracrine signaling. Additionally, the elevated VEGF levels promote endothelial cell proliferation and migration (Fig. 4B–F;

Fig. 7; Fig. S25; Fig. S26), thereby enhancing capillary formation and supplying necessary nutrients for tissue repair. And the reduction in ROS is conducive to endothelial cell migration, angiogenesis, and the differentiation of osteoblasts into mature bone cells, collectively contributing to improved repair of bone defects.

As dynamic living materials, iOB spheroids are capable of interpreting their microenvironment, exhibiting mature osteoblastic functionality, operating as bio-units to produce extracellular matrix components and bioactive signaling cues. The self-generated matrix creates a more natural and supportive 3D microenvironment on adjacent bone tissue, reducing reliance on external bioactive materials (Fig. 8). Although an analysis of the influence of the immunity on the efficiency of our iOB-sp engineering approach remains to be performed, we envision that iOBs or their spheroids could offer design flexibility in creating three-dimensional living materials through their interactions and combinations, making them suitable for autologous applications. Patient-derived iOB cells can be combined with xenogeneic bone scaffolds

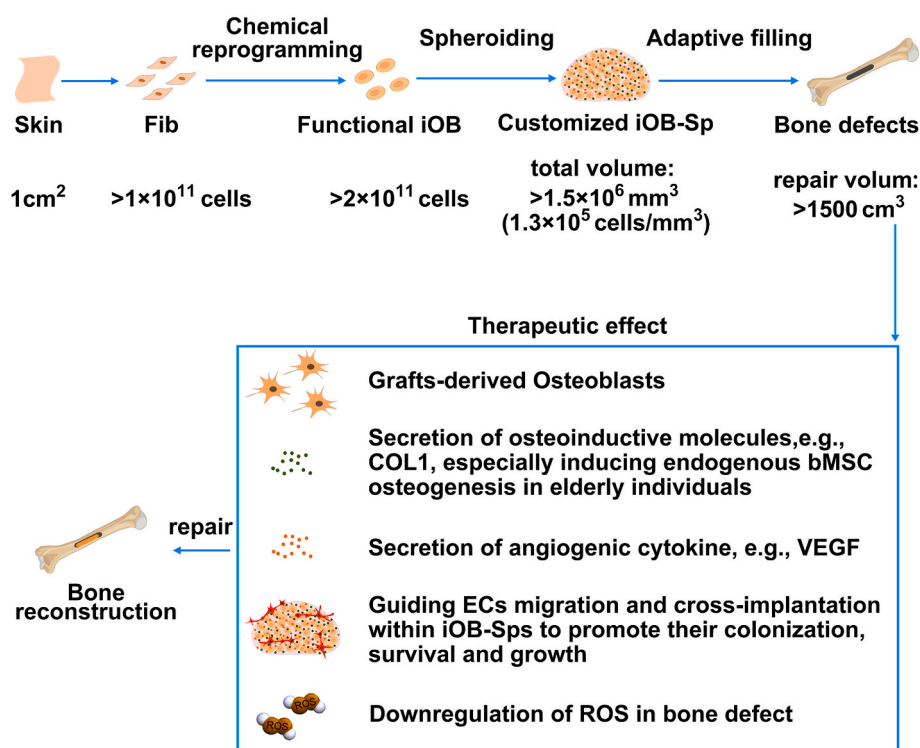


Fig. 8. Schematic showing the role and potential mechanism of iOB-Sps in bone defects repair. Our innovative methodology enables the reprogramming of fibroblasts to generate large quantities of induced osteoblasts and iOB spheroids, which retain the functional characteristics of youthful native osteoblasts, devoid of tumorigenicity, regardless of donor age. This process can yield approximately 2×10^{11} iOBs from a mere 1 cm² skin biopsy—enough to repair around 1500 cm³ of bone tissue defects. These induced osteoblast spheroids, as living, self-scaffolding materials, exhibit improved survival and demonstrate resistance to damage-related stress without functional deterioration, both in vitro and in vivo. They not only mature and achieve self-bone formation in vivo but also accelerate endogenous osteogenesis and local angiogenesis while adapting to their environment, replicating tissue composition, maintaining high cell density to facilitate matrix remodeling, and reducing ROS levels.

without additional extracellular matrix proteins to produce biomaterials with autologous bone characteristics for repairing severe bone defects. These approaches avoid the use of commonly used allogeneic bone materials in clinical practice, reducing the risk of adverse ethical events and accelerating the pace of clinical translation and living material development.

4. Conclusion

In conclusion, the patients' own skin fibroblasts have been engineered through chemical reprogramming and spheroidization techniques for the purpose of bone defect repair. The iOB-Sps, as a novel type of living biomaterial that does not rely on other material components, have been validated for their feasibility in treating bone defects in vivo and providing osteogenic seed cells for effective in vitro composite scaffolding with decellularized porcine bone tissue. This research provides innovative clinical treatment options for refractory bone defects, particularly in elderly patients, suggesting a novel therapeutic direction for addressing age-related bone issues with autologous cell therapy.

5. Materials and methods

5.1. Cell cultures

All cells were isolated from healthy individuals; Informed consents were obtained from all subjects. The collection procedures of skin and bone samples were approved by the Medical Ethics Committee of the Department of Medicine at Kunming University (2016-L-33).

Primary fibroblasts were harvested from leg or abdominal skin of healthy donors with various ages at 38, 39, 67, 70, 74, 75, and 79 years

old. Another fibroblast line from healthy individual of an 8-year-old was harvested from foreskin which was purchased from Millipore (SCC058). No mycoplasma, fungal and bacterial contamination were detected in any of the cells. The primary fibroblasts were started from about 1 cm² skin biopsies. Hair, blood capillary and subcutaneous fat were cleaned from the dermis using scalpel and ophthalmic forceps. Following the previous method for fibroblast isolation [7], the skin specimens were cut into 1 mm² pieces and plated onto 10 cm cell culture treated dishes for cultivation, which allowed fibroblasts to migrate from the explants. Fibroblasts were cultured and expanded in fibroblast medium consisting of high glucose Dulbecco's Modified Eagle Medium (DMEM; Gibco), 10 % fetal bovine serum (FBS; ExCell), 100 U/ml penicillin and 100 µg/ml streptomycin antibiotics (sigma).

Fibroblasts were seeded at $1 \sim 1.5 \times 10^4$ cells per cm² of growth area and incubated at 37.0

°C in humidified 5 % carbon dioxide until 80 % confluent. After reaching confluence, the cells were sub-cultured and counted using trypan blue dye method. These cells were sub-cultured every 3–6 days, continuing the process until they reached the 14th passage.

Bone marrow mesenchymal stem cells (bmSC) were obtained from the bone marrow of healthy individuals following surgery and isolated using the protocol described previously [28], with various ages at 26, 31, 33, 62, 71 and 82 years old.

bmSCs were cultured in MSC medium including low glucose DMEM (Gibco), 8 % fetal bovine serum (FBS) (ExCell), 100 U/ml penicillin and 100 µg/ml streptomycin antibiotics (sigma).

Human umbilical vein endothelial cells (HUVEC) were purchased from ScienCell (#8000). The ECs were cultured in Endothelial Cell Medium (ECM) (ScienCell, #1001). HUVECs at passage P4-P5 were used in vitro testing.

5.2. Induced osteoblasts conversion and cultures

Fibroblasts at passage 13 were used for in vitro induction. For the small molecules screening and their combinations optimization, human fibroblasts were seeded at a density of 1.3×10^4 to $1.8 \times 10^4/\text{cm}^2$ in 10 cm cell culture treated dishes and cultured in fibroblast medium. Small molecules for different signaling pathways were added at the concentrations detailed in Table S1. The cells were incubated with the compounds for 7 days, with media changes every 2–3 days. Different compounds combinations were further used to treat fibroblasts, with the treatment details provided in Table S2.

For the osteoblasts induction, cells were seeded onto 10 cm cell culture treated dishes (700,000–1,000,000 cells/dish) and cultured in fibroblast medium until the cells reached 80 % confluence. Then the cells were transferred to iOB induction medium with chemical cocktails. Specifically, the cells were treated with the CFRVT mixture for 5 days in the first stage, followed by CFRVGSE for 7 days in the second stage, and finally CFRV for 6 days in the third stage.

To confirm the role of WNT signaling pathway in reprogramming, its inhibitors, ICG-001 (5 μM ; MCE) and XAV939 (1 μM ; MCE), were added respectively to the chemical cocktails at all three stages. The treated cells were sampled for further analysis at D0, D5, D12 and D18.

5.3. Osteogenic medium preparation

The osteogenic medium was prepared as described [22], which contained 10 % FBS, supplemented with 10 mM sodium β -glycerophosphate (Sigma-Aldrich), 100 nM dexamethasone (Sigma-Aldrich), and 0.2 mM L-Ascorbic acid (MCE).

5.4. Alizarin red staining method

Staining of calcium nodules was performed according to the instructions provided with the Alizarin Red Staining Kit (OriCell® Alizarin Red Staining Solution, Cyagen, ALIR-10001). Mineralized nodules stained were faded with 10 % cetylpyridinium chloride (Sigma-Aldrich) for 20 min at room temperature. Absorbance at 562 nm of the supernatant was measured using a microplate reader in triplicate. Experiments were repeated three times using the same source of cells.

5.5. iOB spheroids formation

For spheroidal formation of iOBs, which was based on previously reported methods [29], when iOBs reached 80 % confluence, they were dissociated with 0.05 % trypsin. The cells were suspended in osteogenic medium and were aliquoted according to different cell counts, ranging from 7×10^4 to 2×10^6 , corresponding to spheroids of varying sizes. Then they were centrifuged at 300 g for 5 min in V-shaped 15 mL centrifuge tubes. The resultant cell pellets were not to be disturbed and were incubated at 37 °C in humidified 5 % carbon dioxide overnight. Following this incubation, iOB spheroids were formed, which were cultured for 1–5 days for downstream assays, pooling 8 to 10 spheroids per assay.

5.6. H_2O_2 treatment ROS and DCFH-DA detection

In the monolayer culture conditions, iOBs were seeded onto a 6-well plate at a density of 2.5×10^5 in a well. In the spheroid culture, iOBs were spheroidized, with each spheroid containing 2.5×10^5 cells. The following day, both iOBs in monolayer and iOBs spheroids were treated with 800 μM hydrogen peroxide solution (H_2O_2 ; Macklin, H792077) for 4 h at 37 °C in humidified 5 % carbon dioxide. As controls, iOBs in monolayer and iOBs spheroids were treated were not treated with H_2O_2 . After exposure to H_2O_2 , cells were dissociated with 0.05 % trypsin and all cells were collected for counting. Cell viability was determined using the MTS and Acridine orange/propidium iodide (AO/PI) assay (Beijing

BioLab Technology, HR0462). The intracellular ROS levels were evaluated by detecting the oxidative conversion of cell-permeable (2',7'-dichlorodihydrofluorescein diacetate dye (DCFH-DA; Beyotime, S0033S) to fluorescent dichlorofluorescein (DCF). The DCF fluorescence intensity of the cells was measured using a microplate reader (Infinite M200 pro, TECAN) at an excitation wavelength of 488 nm and an emission wavelength of 525 nm. Statistics were obtained from three repeat experiment.

5.7. Cell proliferation assay using MTT staining

HUVECs were either treated with iOB conditioned medium or left untreated in DMEM for 24 h. Then 1×10^3 cells were seeded onto 96-well plates and cultured in ECM for D1, D2, D3, and D4. Cell proliferation was measured with MTT Kit (Beyotime, C0009S) as the manufacturer's protocol. 10 μL of MTT solution (5 mg/mL) was added to each well for 4 h at 37 °C. Then the culture medium was removed and 100 μL of dimethyl sulphoxide (DMSO; Sigma, USA) was added to each well to dissolve the formazan crystals for 30 min. The absorbance at 490 nm was measured using a microplate reader (TECAN, infinite M200 pro). Statistics were obtained from three repeat experiments.

5.8. Collection of cell culture conditioned medium and measurements of paracrine factors

Prepare conditioned media (CM) and iOB secreted protein samples for monolayer cultured iOBs and iOB spheroids in multiple biological replicates (at least three). Cells were plated in 6-well plates (2×10^5 cells/well) or prepared as spheroids (2×10^5 cells/spheroid), both of them were cultured in high glucose DMEM with 10 % FBS. The next day, the culture medium were aspirated and discarded. The cells were washed three times with 2 mL warm PBS and incubated in serum-free, phenol red-free medium containing no protein supplements for 3.5 h (2×10^5 cells/1 mL). After the incubation, the supernatants were centrifuged at 1000 g for 15 min to discard cell debris. The conditioned medium was collected for use in subsequent assays.

The secreted levels of vascular endothelial growth factor (VEGF), Interleukin 6 (IL6) and collagen Type I (COL1) in each sample were measured using the ELISA kits as follows: Human VEGF ELISA Kit (enzyme research, EK-H11892); Human IL6 Kit (Elabscience, E-EL-H6156); Human COL1 ELISA Kit (enzyme research, EK-H10023).

5.9. Indirect co-culture between human bMSCs and iOB-Sp

To establish an indirect co-culture between bMSCs and iOB-Sp, bMSCs sourced from individuals of different ages were seeded into a 24-well plate (2.4×10^4 cells/well), and the iOB-Sp, including 1.3×10^5 cells, was cultured in the transwell insert (NEST, 725111), which was placed in the aforementioned 24-well plate. Both of them were cultured in osteogenic medium for 14 days. After co-cultured, bMSCs were detected using alizarin red staining. As a blank control, bMSCs were plated separately in a 24-well plate without any inserts and cultured in osteogenic medium for 14 days.

5.10. In vitro endothelial cell tube formation assay

HUVECs were either treated with iOB-Sp conditioned medium or maintained in DMEM for 24 h before the cord formation assay. EC tube formation assay was conducted as described [30]. 8×10^4 HUVECs were seeded in a well of 24-well plate on pre-solidified Matrigel (Corning, 354230) and cultured in ECM. The cells were incubated for 24 h at 37 °C and 5 % CO_2 in a humidified atmosphere. The vascular network was photographed through phase contrast microscopy (Olympus). Quantification of tube networks was performed using ImageJ with the Angiogenesis Analyzer plugin.

5.11. Migration assay for HUVECs

To establish a contact-based model for HUVECs and iOBs coculture, 1.5×10^5 HUVECs were formed into spheroid using the hanging drop method as described [29] and then embedded into 35 μ L Matrigel (Corning, 354230) containing uniformly distributed 2×10^5 iOB single cells which were labeled with GFP lentivirus. As a control, an EC spheroid was embedded into 35 μ L Matrigel without iOBs. These cells were cultured in ECM for 3 days and then fixed in 4 % PFA for further frozen section. Sections were stained with hematoxylin-eosin (H&E), or primary antibodies anti-CD31, anti-GFP and DAPI. The linear distances migrated by individual EC cells from their starting spheroid were calculated using ImageJ. ECs located within a direct distance of about 550 μ m from the edge of the spheroid to beyond its surface were analyzed. Statistics were obtained from three repeat experiment.

To establish a non-contact-based model for HUVECs and iOBs coculture, about 2×10^5 HUVECs were formed into a toroid-shaped spheroid, and 2×10^5 iOBs were assembled into a spheroid. Then the toroid-shaped EC spheroid and iOB spheroid were embedded into one 35 μ L Matrigel sphere with a gap about 400 μ m between them. The cells were cultured in ECM for 35 days and were periodically imaged on a Leica bright-field microscope. After co-cultured, the EC spheroid was collected and then fixed in 4 % PFA for further frozen section. Sections were stained with H&E, or primary antibody anti-CD31 and DAPI. Data analysis was conducted based on three repeated experimental trials.

5.12. RT-qPCR detection

Quantitative real-time PCR was employed for osteoblast-associated genes. Total RNA was extracted using RNAiso plus (TAKARA) and 1 μ g of RNA was reverse transcribed into cDNA using PrimeScript RT reagent Kit with gDNA Eraser (TAKARA). Real-time RT-PCR was carried out using Real-time PCR Master Mix (TAKARA) on the ABI QuantStudio 5 Real-Time PCR System. All values (mean \pm SD) were normalized with respect to the β -actin mRNA level in each sample, and relative expression for each target gene was evaluated the Δ CT and $2^{-\Delta\Delta$ CT method. Genes and primer sequences are listed in the [Supplementary Table S3](#).

Dot plots showing gene expression were produced using the ggplot2 package in R. The colour of each circle reflects the log2 Foldchange ($-\Delta\Delta$ CT value) which is relative to untreated cells or D18 treated cells.

5.13. Western blotting

Cells were ground with liquid nitrogen and lysed with cell lysis buffer RIPA (Beyotime, Cat. No. P0013B). After cell lysis, the supernatant was collected by centrifugation at 4 $^{\circ}$ C, 12000 rpm for 15 min. Equal amounts of protein were separated by 10 % SDS-PAGE gel (Beyotime, Cat. No. P0012AC) electrophoresis and transferred to PVDF membrane (Sigma, Cat. No. 3010040001). The membrane was blocked with 5 % BSA in Tween20 (TBS-T) at room temperature for 1 h. The membrane was incubated with the following antibodies respectively: β -actin (santa Cruz, sc-69879), CTNNB1 (Medchem EXPress, HY-P80488), WNT5A (GeneTex, GTX111187), c-MYC (Proteintech, 67447-1-Ig), SP7(abcam, ab94744), DLX5 (Proteintech, 67111-1-Ig), RUNX2 (santa Cruz, sc-39035) primary antibody on a shaker at 4 $^{\circ}$ C overnight. After washing the membrane with TBS-T, it was incubated with Goat Anti-Mouse IgG (H + L), HRP Conjugate secondary antibody (Transgen, HS201-01), or Goat Anti-Rabbit IgG (H + L), HRP Conjugate secondary antibody (Transgen, HS101-01) at room temperature for 1 h, and then imaged according to the manufacturer's instructions using a chemiluminescence kit (Sunviewbio, PL101-100).

5.14. Senescence-associated β -galactosidase (SA- β -Gal) assay

Cells were washed twice with PBS then fixed with 4 % Paraformaldehyde (PFA) in PBS for 6 min. Cells were rinsed three times with

PBS before staining and then incubated in SA- β -gal staining solution with Cell Senescence SA- β -Gal Staining Kit (Beyotime, C0602) according to the manufacturer's protocol. Stained cells were monitored under a Leica bright-field microscope. Statistics were obtained from three repeat experiments. Nuclei were labeled with DAPI 1 μ g/ml (Life Technologies) and SA- β -gal positive cells were counted manually.

5.15. Decellularized porcine bone preparation and coculture with iOBs or iOB-Sp

Decellularized porcine cancellous bone were generated as described [31–33]. In brief, cancellous bone from the femoral shaft of 1-year-old healthy pigs was used. Soft tissue, bone marrow, and cartilage were removed. The bones were cut into cuboid-shaped sticks measuring 8 \times 5 \times 5 mm. Blood and bone marrow tissues were further eliminated by rinsing with water at 70 $^{\circ}$ C three times. Cells and proteins were subsequently removed by immersing the samples in 0.5 % Triton X-100 and 10 % sodium chloride, followed by treatment with a 1:1 (v/v) mixture of chloroform and methanol for 12 h, and then with a 30 % hydrogen peroxide solution for another 12 h. For the interval between each of the aforementioned steps, the samples were washed with running water for 30–60 min. The bone granules were then immersed in 0.5 mol/L hydrochloric acid (HCl) for 5 min. The processed pig cancellous bone granules were washed with running warm deionized water for 1 h. Finally, the decellularized porcine bone was freeze-dried, sterilized using irradiation, and stored at -80° C in sterile tubes until further use.

The decellularized porcine bone was used solely for in vitro coculture with iOBs. 5×10^5 iOB single cells or two iOB spheroids, each containing 2.5×10^5 cells, were resuspended in 100 μ L of osteogenic medium and subsequently placed in decellularized bone. The spheroids were embedded in the pores of the decellularized bone, while the single cells were fully encapsulated on the dense surface of the trabecular bone. The samples were incubated at 37 $^{\circ}$ C in humidified 5 % carbon dioxide for 30 min to ensure attachment of the cells with bone tissue, while maintaining moisture in the bone throughout this period. After this incubation, the single cells were not washed away, and fresh osteogenic medium was added to the co-culture dish. The co-culture of iOBs and decellularized bone was maintained for 5 days. Then the bone grafts were washed with PBS and fixed in 4 % PFA for downstream assays.

5.16. Transcriptome analysis

RNA-seq libraries were prepared from samples that passed QC according to the manufacturer's protocol (Illumina). Sequencing to produce pair-end 150-bp reads was then performed on an Illumina novaseq instrument. Hisat2 v2.2.1 was used for building the genome index, and Clean Data was mapped to the reference genome using Hisat2 v2.2.1. Stringtie

v 2.1.7 was used for transcriptome expression estimation. Reads Count for each gene in each sample was counted by python scripts. Each analysis was conducted with at least five biological replicates in each group.

Transcripts Per Million (TPM) of each gene is calculated based on the length of the gene and the number of reads mapped to that gene, while normalizing across all genes in the sample, allowing for direct comparison of gene expression levels both within and across samples.

The 43 genes associated with osteogenesis [8,22,34] were selected and plotted in a heat-map using ComplexHeatmap package in R. The correlation coefficient was calculated output with R-platform.

Principle Component Analysis(PCA)was performed on whole transcriptome without gene selections via FactoMine R package.

DESeq2 was used to detect differentially expressed genes between two comparison groups for samples with biological duplicates. Genes with P-values <0.05 were found to be assigned as differentially expressed by DESeq2.

KEGG pathway enrichment statistics of differentially expressed

genes were achieved by clusterProfiler software, and KEGG pathways with $P < 0.05$ were set as significant enrichment results.

Chord plot was produced using SolarGenomic to visually represent the enrichment of specific differentially expressed genes. In the GO_Circos plot, the left half displays a heatmap of the differentially expressed genes, where blue indicates downregulation (darker shades represent stronger downregulation) and red indicates upregulation (darker shades represent stronger upregulation). The right half of the plot shows the GO terms, with ribbons connecting the genes to their corresponding GO terms.

After removing genes with counts <15 in more than 75 % of the samples in the transcriptome data, 12644 genes were passed to weighted gene co-expression network analysis (WGCNA) via WGCNA R package. Power of 20 is interpreted as a soft-threshold of the correlation matrix.

The transcriptome raw data are available at NCBI Gene Expression Omnibus (GEO) (www.ncbi.nlm.nih.gov/geo/), accession ID: GSE278288 and GSE278615.

5.17. Molecular interaction network

Transcriptome data in the three modules (turquoise, brown and yellow) with the highest correlation in WGCNA analysis were used to produce correlation network. Spearman correlation coefficients were calculated between various genes in these modules to obtain the correlation coefficient matrix (R matrix) and the P-value matrix (P matrix) using Hmisc package in R. Then the genes used for the molecular interaction network were filtered based on the following criteria: 1), the genes were differentially expressed with a \log_2 Foldchange ≥ 2 and $P < 0.05$; 2), There is a notable correlation ($R > 0.75$, $P < 0.05$) with either RUNX2 in the yellow module, WNT5A in the turquoise module, or MYC in the brown module; 3), There is a direct connection with either RUNX2, WNT5A, or MYC in STRING database. In the filtered gene list, the top ten genes most strongly associated with RUNX2, WNT5A, and MYC, respectively, were used to construct a network connectivity map. If fewer than ten genes were found for any, all were included. The final network was generated using Cytoscape with a threshold of $R > 0.75$, and edges that were not confirmed in the STRING database were removed.

5.18. Surgical procedure and cell transplantation

All animal studies were approved by the Experimental Animal Welfare Ethics Committee of Kunming University (KMU2021022) and conducted in accordance with animal ethics guidelines. Male NOD/SCID mice (aged 8–12 weeks) were obtained from Beijing Huafukang Company. All efforts were made to minimize animal suffering as well as the number of rodents utilized. 5 animals per group were used. A femoral defect model was used as previously reported [22]. Briefly, under isoflurane anesthesia (induction: 5 %, maintenance 1.5 %), incision of skin and subcutaneous tissues was performed to expose the muscle white line, which provided sufficient exposure of femur mid-diaphysis by blunt separation in rectus femoris and semitendinosus. Centered proximal intersection of the right side of the femur was performed. A 5 mm in the length and 1.5 mm in width femoral bone defect was created by dental drill on the right femur. Human fibroblasts (Fibs), bMSCs from young individual, and iOB-Sps from old donor were stained with Hoechst 33342 (Thermo, NucBlue live cell) or labeled with EGFP lentivirus. Single suspended Fibs or bMSCs were mixed with Matrigel (Corning, 354230) and transplanted into the lesion site at a dose of 5×10^5 cells/mouse. Four spheroids, each containing 1.3×10^5 iOB cells or fibroblasts, were transplanted into the lesion site/mouse. 28 days after transplantation, mice were euthanized. Thighs were dissected, fixed with 4 % PFA for the following analysis.

For securing the spheroids to the bone defect site: cell spheroids are carefully positioned and fixed within the concave region of the bone defect to prevent any movement in any direction (anterior, posterior,

superior, or inferior) during the surgical procedure. The adjacent muscle is meticulously closed to ensure that the muscle layer completely envelops the defect, thereby preventing the graft from dislodging from the concavity during suturing. Finally, the skin is tightly sutured to ensure that the mouse does not disturb the surgical suture line.

5.19. Tissue collection

Mice were euthanized using Carbon Dioxide (CO_2). Mice that need to be sacrificed were put into the euthanasia chamber and the CO_2 flow rate displaced 30 % of the chamber volume per minute. Gas flow was maintained for at least 1 min after apparent clinical death. Then the bone tissue was collected and placed in 4 % PFA for further processing.

5.20. Detection of ROS levels in bone defect areas

ROS levels in bone defect post 28 days transplantation were detected using mouse ROS ELISA kit according to the manufacturer's protocol (mlbio, YJ141325). Briefly, fresh bone tissue from the defect area was collected, and the surrounding muscle was carefully removed. The bone tissue was weighted and an appropriate amount of physiological saline was added. The tissue was then homogenized thoroughly. Following this, the mixture was centrifuged at 3000 g for 10 min, and the supernatant was collected. The assay was performed according to the instructions provided in the reagent kit, and the Optical Density (O.D.) was measured at 450 nm using a microtiter plate reader (Infinite M200 pro, TECAN).

ROS Brite™ 700 was used to assess the mice femur defect model 7 days after surgery [35]. Bioluminescence imaging was performed to evaluate ROS production in the defect area. Mice were anesthetized with isoflurane, and ROS Brite™ 700 (in vivo imaging solutions, 100 μM in Hanks' solution with 20 mM HHBS) was injected into the defect region. Bioluminescence images were then acquired using an in vivo imaging system (PerkinElmer, Boston, USA).

5.21. Detection of bone mineral density

The complete right femur of the mice was collected and fixed in a 4 % PFA. Muscle and connective tissue were peeled off before analysis. For the examination, the specimens were placed in Micro-CT sample cups and scanned using a Micro-CT scanner (Bruker, SkyScan1272) under the same conditions followed by three-dimensional reconstruction. Measurements were taken for bone mineral density (BMD), trabecular number (Tb. N), trabecular separation (Tb. Sp), bone surface (BS), bone volume (BV), and tissue volume (TV), and the relative bone volume fraction (BV/TV) was calculated.

5.22. Histochemical staining

Bone tissue samples were decalcified in 0.5 M EDTA (Servicebio, G1105) for 12–14 days. Frozen sections of tissue were prepared. Sections were staining with Alizarin Red Staining Kit (Cyagen, ALIR-10001), Modified Saffron-O and Fast Green Stain Kit for bone (solarbio, G1371), and H&E staining kit (Phygene, PH0516) by corresponding staining kit instructions.

5.23. Immunohistochemistry staining and quantification analysis

The staining reagents, including antibodies, were provided in detail as follows: anti-GFP (1:600; Abcam, ab13970), anti-IBSP(1:300; reactivity with Human, Mouse; Bioss, bs-2668R), anti-OCN (1:100; reactivity with Human, Mouse; Bioss, bs-4917R), anti-Ki67 (1:200; reactivity with Human, Mouse; Invitrogen, 2747806), anti-SP7 (1:150; reactivity with Human; Abcam, ab94744), anti-RUNX2 (1:200; reactivity with Human, Mouse; santacruz, sc-390351), anti-COL1 (1:400; reactivity with Human, Mouse; Bioss, bs-0578R), anti-VEGF (1:50; reactivity with

Human, Mouse; santacruz, sc-7269), human-specific anti-VEGF (pre-diluted; reactivity with Human; Abcam, ab27620), anti-STEM121 (1:250; reactivity with Human specific; TAKARA, Y40410) and anti-CD31 (1:400; reactivity with Human, Mouse; Immunoway, YP0530; or 1: 400; reactivity with Mouse; Servicebio, GB12063), Nrf2 (1:500; reactivity with Human, mouse, rat; Proteintech, 80593-1-RR, Lot:23013625); secondary antibodies (Invitrogen, A21235, A21244; Univ, 703-545-155, 711-165-152; Abcam, AB150159; Servicebio, GB21301). Tunel (Beyotime; C1090), DAPI (Life Technologies, 62248). All of them were utilized in accordance with the manufacturer's instructions. For negative controls, immunostaining with no primary antibodies was performed.

For immunofluorescent staining *in vitro*, cells plated on cell climbing sheets (solarbio, YA0350) in 24-well plates were fixed by 4 % PFA solution for 10 min and then changed to PBS at room temperature. Cells were then treated with 0.1 % Triton X-100 for 10 min, followed by incubation in a blocking buffer (3 % bovine serum albumin in PBS) for 30 min. Afterward, samples were incubated with primary antibodies at 4 °C overnight and then with an appropriate fluorescent probe conjugated with secondary antibodies for 2 h at RT. Nuclei were counter-stained with 4', 6-diamidino-2-phenylindole (DAPI). Images were captured with a fluorescence microscope SLIDEVIEW (VS200, OLYMPUS). The analyses were conducted in accordance with previously described methods [36]. For quantification of positive cell percentages, at least 5 regions in each tissue section image were randomly picked, and each image was assessed for the number of DAPI positive nuclei, followed by the enumeration of cells expressing the positive biomarkers of interest. Statistics were obtained from three independent experiments.

For the immunohistochemistry analysis for bone defect area, the fixed femurs were decalcified in 0.5 M EDTA (Servicebio, G1105) for 12–14 days. Then they were transferred to a sucrose solution of gradually increasing concentration for 48–72 h. The bone samples were embedded in O.C.T. (Sakura-Finetek). Each sample was sequentially sliced into 10 µm thick sections using an HM525 NX Cryostat (Thermo Fisher Scientific) to acquire serial bone tissue sections. Sections were incubated overnight with primary antibodies at 4 °C overnight. The sections were rinsed with phosphate buffered saline (PBS) twice, followed by incubation with the corresponding secondary antibodies at room temperature for 2 h and then rinsed with PBS. Finally, the slices were covered with DAPI and images were captured using a microscope SLIDEVIEW (VS200, OLYMPUS).

To quantify cells with markers of interest *in vivo*, a set of sections was selected for staining based on the sampling method: one slice was taken after every four intervening slices from all slices exhibiting transplanted cell signals. Corresponding slices were also selected for staining analysis in the control group. The sections per bone tissue from 3 to 6 animals were analyzed using ImageJ (1.46 version). To ensure consistent and reliable quantification of immunofluorescence microscopy images *in vivo*, image recording was performed under the same scanning conditions for all the samples in the same experiment, which included objective lens, illumination intensity, emission window, digital zoom, scanning speed, and offset and gain settings. All quantifications were performed blinded, referencing the method as described [37]. For counting iOBs after transplantation, all GFP positive cells in the femoral shaft, both in and around the cell transplantation area, were quantified. For the analysis and quantification of cell death or cell proliferation by Tunel assay or Ki67 immunohistochemistry staining, all GFP positive cells, Tunel and GFP double-positive cells or Ki67 and GFP double-positive cells in the femoral shaft, were quantified; The final results presented the proportion of double-positive cells among the GFP-positive cells. The IBSP-positive cells within the total GFP + cell population were determined by quantifying the total number of GFP-expressing cells and subsequently counting the cells that were double-labeled with GFP and IBSP across at least eight random fields in each section image. For the COL1 or IBSP positive signals analysis, the area percentage of COL1 or IBSP in the bone defect healing area were

calculated. For quantifications of percentage of VEGF or CD31 positive cells, the number of DAPI positive nuclei was scored, followed by counting the number of cells expressing VEGF or CD31 in at least eight random fields in each section image.

5.24. Teratoma formation assay in NOD/SCID mice

Male immunodeficient NOD/SCID mice aged 8–10 weeks were used. HEK293T cells or iOBs were harvested at 1×10^7 , mixed with Matrigel (Corning, 354230) in a 1:1 ratio, and injected at a volume of 200 µL subcutaneously. Mice were euthanized at sampling time point, and excised tumors or implants were fixed in 4 % PFA (Sigma-Aldrich) and sectioned. Sections were stained with hematoxylin-eosin, and analyzed histologically.

5.25. Statistical analysis

The experiments were conducted at least three times independently ($n = 3$), and statistical analysis was performed using SPSS version 24. To assess statistical significance, two-group comparisons were analyzed using Student t-test, while multiple-group comparisons were analyzed using one-way analysis of variance (ANOVA) with Bonferroni correction. A p-value below 0.05 was considered statistically significant.

CRediT authorship contribution statement

Yanjiao Li: Writing – review & editing, Supervision, Project administration, Methodology, Investigation, Conceptualization. **Bin Jiang:** Writing – review & editing, Supervision, Methodology. **Zhen Wu:** Methodology, Investigation. **Zhaoxia Ma:** Investigation. **Lihua Qiu:** Investigation. **Wen Cui:** Investigation. **Yunhui Zhao:** Investigation. **Jinghe Yan:** Methodology, Investigation. **Daiping Ma:** Investigation. **Xingfei Wu:** Investigation. **Shu Liang:** Investigation. **Sitao Wang:** Investigation. **Yanqun Zhao:** Investigation. **Mengting Wang:** Investigation. **Min Hu:** Writing – review & editing, Supervision, Project administration, Methodology, Investigation, Funding acquisition, Conceptualization.

Ethics approval and consent to participate

All cells were isolated from healthy individuals; Informed consents were obtained from all subjects. The collection procedures of skin and bone samples were approved by the Medical Ethics Committee of the Department of Medicine at Kunming University (2016-L-33).

All animal studies were approved by the Experimental Animal Welfare Ethics Committee of Kunming University (KMU2021022) and conducted in accordance with animal ethics guidelines.

Declaration of competing interest

The authors declare the following personal relationships which may be considered as potential competing interests: Bin Jiang is currently employed by R&D Division, Eureka Biotech Inc. Zhen Wu, Daiping Ma and Mengting Wang are currently employed by Shenzhen Zhendejici Pharmaceutical Research and Development Co., Ltd. Wen Cui, Yunhui Zhao, Xingfei Wu, Shu Liang, Sitao Wang and Yanqun Zhao are currently employed by Yunnan Jici Institute for Regenerative Medicine Co., Ltd. Wen Cui and Xingfei Wu are currently employed by Guangzhou Dayi Pharmaceutical Research Co., Ltd. The authors declare the following personal relationships which may be considered as potential competing interests: icurrently employed by R&D Division, Eureka Biotech Inc.

Acknowledgments

This work was supported by the funding of Yunnan Key Laboratory of Basic Research for Bone and Joint Diseases (202205AG070075) and

Science & Technology Department of Yunnan Province (2016RA093).

Appendix A. Supplementary data

Supplementary data to this article can be found online at <https://doi.org/10.1016/j.bioactmat.2025.04.021>.

References

- [1] Office of the Surgeon, G. Reports of the surgeon general, in: *Bone Health and Osteoporosis: A Report of the Surgeon General*, Office of the Surgeon General, 2004 (US).
- [2] A. Chandra, J. Rajawat, Skeletal aging and osteoporosis: mechanisms and therapeutics, *Int. J. Mol. Sci.* 22 (7) (2021), <https://doi.org/10.3390/ijms22073553>.
- [3] M. Barba, C. Cicone, C. Bernardini, et al., Adipose-derived mesenchymal cells for bone regeneration: state of the art, *BioMed Res. Int.* 2013 (2013) 416391, <https://doi.org/10.1155/2013/416391>.
- [4] A.T.P. Souza, G.P. Freitas, H.B. Lopes, et al., Effect of cell therapy with allogeneic osteoblasts on bone repair of rat calvaria defects, *Cytotherapy* 20 (10) (2018) 1267–1277, <https://doi.org/10.1016/j.jcyt.2018.06.010>.
- [5] E. Potier, E. Ferreira, A. Meunier, et al., Prolonged hypoxia concomitant with serum deprivation induces massive human mesenchymal stem cell death, *Tissue Eng.* 13 (6) (2007) 1325–1331, <https://doi.org/10.1089/ten.2006.0325>.
- [6] Q. Li, P. Lan, Activation of immune signals during organ transplantation, *Signal Transduct. Targeted Ther.* 8 (1) (2023) 110, <https://doi.org/10.1038/s41392-023-01377-9>.
- [7] L.I. Hushchtscha, C.E. Napier, J.R. Noble, et al., Enhanced isolation of fibroblasts from human skin explants, *Biotechniques* 53 (4) (2012) 239–244, <https://doi.org/10.2144/0000113939>.
- [8] J.Y. Yoon, N. Mandakhbayar, J. Hyun, et al., Chemically-induced osteogenic cells for bone tissue engineering and disease modeling, *Biomaterials* 289 (2022) 121792, <https://doi.org/10.1016/j.biomaterials.2022.121792>.
- [9] Y. Takeda, Y. Harada, T. Yoshikawa, P. Dai, Chemical compound-based direct reprogramming for future clinical applications, *Biosci. Rep.* 38 (3) (2018), <https://doi.org/10.1042/bsr20171650>.
- [10] Y.X. Zhang, S.L. Chen, Y.M. Li, Y.W. Zheng, Limitations and challenges of direct cell reprogramming in vitro and in vivo, *Histol. Histopathol.* 37 (8) (2022) 723–737, <https://doi.org/10.14670/hh-18-458>.
- [11] J. Wang, S. Sun, H. Deng, Chemical reprogramming for cell fate manipulation: methods, applications, and perspectives, *Cell Stem Cell* 30 (9) (2023) 1130–1147, <https://doi.org/10.1016/j.stem.2023.08.001>.
- [12] J. Ma, S.K. Both, F. Yang, et al., Concise review: cell-based strategies in bone tissue engineering and regenerative medicine, *Stem. Cells. Transl. Med.* 3 (1) (2014) 98–107, <https://doi.org/10.5966/sctm.2013-0126>.
- [13] G.J. Meijer, J.D. de Bruijn, R. Koole, C.A. van Blitterswijk, Cell-based bone tissue engineering, *PLoS Med.* 4 (2) (2007) e9, <https://doi.org/10.1371/journal.pmed.0040009>.
- [14] A. Fallah, A. Beke, C. Oborn, et al., Direct reprogramming of fibroblasts to osteoblasts: techniques and methodologies, *Stem. Cells. Transl. Med.* 13 (4) (2024) 362–370, <https://doi.org/10.1093/stcltm/szad093>.
- [15] R. Vlasi, X. Zhang, M. Wu, G. Chen, Wnt signaling: Essential roles in osteoblast differentiation, bone metabolism and therapeutic implications for bone and skeletal disorders, *Genes Dis.* 10 (4) (2023) 1291–1317, <https://doi.org/10.1016/j.gendis.2022.07.011>.
- [16] X. Han, H. Yu, D. Huang, et al., A molecular roadmap for induced multi-lineage trans-differentiation of fibroblasts by chemical combinations, *Cell Res.* 27 (6) (2017) 842–843, <https://doi.org/10.1038/cr.2017.77>.
- [17] I.N. Saburina, A.A. Gorkun, A.F. Fidarov, et al., Induction of vasculo- and osteogenesis in spheroids formed by adipose-derived stromal cells, *Bull. Exp. Biol. Med.* 166 (1) (2018) 163–169, <https://doi.org/10.1007/s10517-018-4306-4>.
- [18] A. Salhotra, H.N. Shah, B. Levi, et al., Mechanisms of bone development and repair, *Nat. Rev. Mol. Cell Biol.* 21 (11) (2020) 696–711, <https://doi.org/10.1038/s41580-020-00279-w>.
- [19] A. Takeno, I. Kanazawa, M. Notsu, et al., Inhibition of adenosine monophosphate-activated protein kinase suppresses bone morphogenetic protein-2-induced mineralization of osteoblasts via Smad-independent mechanisms, *Endocr. J.* 65 (3) (2018) 291–298, <https://doi.org/10.1507/endocrj.EJ17-0229>.
- [20] Q. Jin, Y. Liu, Z. Zhang, et al., MYC promotes fibroblast osteogenesis by regulating ALP and BMP2 to participate in ectopic ossification of ankylosing spondylitis, *Arthritis Res. Ther.* 25 (1) (2023) 28, <https://doi.org/10.1186/s13075-023-03011-z>.
- [21] A.Y. Chen, C. Zhong, T.K. Lu, Engineering living functional materials, *ACS Synth. Biol.* 4 (1) (2015) 8–11, <https://doi.org/10.1021/sb500113b>.
- [22] K. Yamamoto, T. Kishida, Y. Sato, et al., Direct conversion of human fibroblasts into functional osteoblasts by defined factors, *Proc. Natl. Acad. Sci. U. S. A.* 112 (19) (2015) 6152–6157, <https://doi.org/10.1073/pnas.1420713112>.
- [23] B. Jiang, L. Yan, Z. Miao, et al., Spheroidal formation preserves human stem cells for prolonged time under ambient conditions for facile storage and transportation, *Biomaterials* 133 (2017) 275–286, <https://doi.org/10.1016/j.biomaterials.2017.03.050>.
- [24] P. Rybkowska, K. Radoszkiewicz, M. Kawalec, et al., The metabolic changes between monolayer (2d) and three-dimensional (3d) culture conditions in human mesenchymal stem/stromal cells derived from adipose tissue, *Cells* 12 (1) (2023), <https://doi.org/10.3390/cells12010178>.
- [25] S. Regmi, P.K. Raut, S. Pathak, et al., Enhanced viability and function of mesenchymal stromal cell spheroids is mediated via autophagy induction, *Autophagy* 17 (10) (2021) 2991–3010, <https://doi.org/10.1080/15548627.2020.1850608>.
- [26] S. Bou-Ghannam, K. Kim, D.W. Grainger, T. Okano, 3D cell sheet structure augments mesenchymal stem cell cytokine production, *Sci. Rep.* 11 (1) (2021) 8170, <https://doi.org/10.1038/s41598-021-87571-7>.
- [27] M.F. Desantis-Desantis, J.D. Rivas-Carrillo, S. Sánchez-Enríquez, Protective role of osteocalcin in diabetes pathogenesis, *J. Bone Miner. Metab.* 38 (6) (2020) 765–771, <https://doi.org/10.1007/s00774-020-01130-0>.
- [28] X. Wang, E.A. Kimbrel, K. Ijichi, et al., Human ESC-derived MSCs outperform bone marrow MSCs in the treatment of an EAE model of multiple sclerosis, *Stem Cell Rep.* 3 (1) (2014) 115–130, <https://doi.org/10.1016/j.stemcr.2014.04.020>.
- [29] S.Y. Lee, I.S. Koo, H.J. Hwang, D.W. Lee, In Vitro three-dimensional (3D) cell culture tools for spheroid and organoid models, *SLAS Discov.* 28 (4) (2023) 119–137, <https://doi.org/10.1016/j.slasdisc.2023.03.006>.
- [30] K.L. DeCicco-Skinner, G.H. Henry, C. Cataisson, et al., Endothelial cell tube formation assay for the in vitro study of angiogenesis, *J. Vis. Exp.* 91 (2014) e51312, <https://doi.org/10.3791/51312>.
- [31] T. Woods, P.F. Gratzner, Effectiveness of three extraction techniques in the development of a decellularized bone-anterior cruciate ligament-bone graft, *Biomaterials* 26 (35) (2005) 7339–7349, <https://doi.org/10.1016/j.biomaterials.2005.05.066>.
- [32] A.M. Matuska, M.F. Dolwick, P.S. McFetridge, Approaches to improve integration and regeneration of an ex vivo derived temporomandibular joint disc scaffold with variable matrix composition, *J. Mater. Sci. Mater. Med.* 29 (10) (2018) 152, <https://doi.org/10.1007/s10856-018-6164-z>.
- [33] P. Lei, R. Sun, L. Wang, et al., A new method for xenogeneic bone graft deproteinization: comparative study of radius defects in a rabbit model, *PLoS One* 10 (12) (2015) e0146005, <https://doi.org/10.1371/journal.pone.0146005>.
- [34] S. Hochmann, K. Ou, R. Poupardin, et al., The enhancer landscape predetermines the skeletal regeneration capacity of stromal cells, *Sci. Transl. Med.* 15 (688) (2023) eabm7477, <https://doi.org/10.1126/scitranslmed.abm7477>.
- [35] H. Sun, J. Xu, Y. Wang, et al., Bone microenvironment regulative hydrogels with ROS scavenging and prolonged oxygen-generating for enhancing bone repair, *Bioact. Mater.* 24 (2023) 477–496, <https://doi.org/10.1016/j.bioactmat.2022.12.021>.
- [36] S. Kriks, J.W. Shim, J. Piao, et al., Dopamine neurons derived from human ES cells efficiently engraft in animal models of Parkinson's disease, *Nature* 480 (7378) (2011) 547–551, <https://doi.org/10.1038/nature10648>.
- [37] J. Chen, U. Sivan, S.L. Tan, et al., High-resolution 3D imaging uncovers organ-specific vascular control of tissue aging, *Sci. Adv.* 7 (6) (2021), <https://doi.org/10.1126/sciadv.abd7819>.